Tel Aviv University

Raymond & Beverly Sackler School of Physics & Astronomy

Nonlinear Signal Generation from Nanoparticles

In partial fulfillment to the requirements for the degree of

Master of Science at Tel Aviv University

Department of Condensed Matter Physics

By

Ilan Sher

Under the supervision of Prof. Haim Suchowski

June 2019

Abstract

Nonlinear Optics (NLO) is a phenomenon where the medium's optical response is not proportional to the applied optical field. It has been observed just after the laser was introduced by T. Maiman. The early attempt to give theoretical ground to NLO was made by introducing perturbations in harmonic oscillator model. This nonlinear harmonic oscillator model have yielded good results in predicting material's nonlinear response for variety of materials with different crystallographic configurations.

Recently, however, it was found experimentally that for metamaterials with changing geometry, nonlinear oscillator model cannot predict optimal geometry for Second Harmonic Generation (SHG). On the other hand, it was shown that nonlinear scattering theory is consistent with their experiment results. Within this theory, not only amplitude of generated nonlinear SH signal contributes to measurement, but also relative phase between different points on the structure. As a result, the strongest surface second harmonic (SH) response does not necessarily give the strongest nonlinear signal in the detector placed in Far Field.

The goal of this work was to observe SHG signal from the nanostructures surface, e.g. in the nearfield regime by utilizing Scanning Near Field Optical Microscopy (SNOM) with Ultra-Fast Femto Second laser. Observing strong SH signal on the near field of a nanobar would provide a proof of the nonlinear scattering theory since according to this theory such nanostructure exhibits strong near-field SH that cancels out in the Far-Field due to the phase relationship. Such a near-field observation will firmly ground a theory that has been so far confirmed by Far-Field measurements and will open the way to the design of meta-materials with desired nonlinear properties.

Acknowledgments

Foremost, I would like to express my sincere gratitude to my advisor Prof. Haim Suchowski for the continuous support of my study and research, for his patience, motivation, enthusiasm, and immense knowledge. I am grateful to all the members of the Femto-Nano Laboratory and especially to Dr. Michael Mrejen and Uri Arieli, for steering me in the right direction whenever I needed it.

Finally, I must express gratitude to my parents and to my family and friends for providing me with support and encouragement throughout my study. Thank You.

Contents

1. Theoretical background

1.1 Nonlinear Optics Introduction

Nonlinear optics is a branch of optics, where the medium optical response goes beyond the linear proportionality to the applied EM field. Typically, this occurs when the input laser is strong enough to change material's optical property. The first observed nonlinear effect was second-harmonic generation (SHG) discovered by P. Franken just a year after the first laser was introduced by T. Maiman. In this chapter, I follow the discussion described in chapter 1-2 in Ref. [1].

In conventional optics the medium response known as polarization $\boldsymbol{P}(t)$ to the EM field $\boldsymbol{E}(t)$ is described by the induced polarization as follows:

$$\boldsymbol{P}(t) = \epsilon_0 \boldsymbol{\chi}^{(1)} \boldsymbol{E}(t) \tag{1.1}$$

Where $\chi^{(1)}$ is the *linear susceptibility and* ϵ_0 is vacuum permittivity. In the nonlinear regime, the polarization is expanded to further orders in $E(t)$ as follow:

$$\begin{aligned} \boldsymbol{P}(t) &= \epsilon_0 \left[\boldsymbol{\chi}^{(1)} \boldsymbol{E}(t) + \boldsymbol{\chi}^{(2)} \boldsymbol{E}^2(t) + \boldsymbol{\chi}^{(3)} \boldsymbol{E}^3(t) + \cdots \right] \\ &= \boldsymbol{P}^{(1)}(t) + \boldsymbol{P}^{(2)}(t) + \boldsymbol{P}^{(3)}(t) + \cdots \end{aligned} \tag{1.2}$$

Equivalently, $\chi^{(n)}$ is called $n - order$ susceptibility and in general it's a n+1 rank tensor. The scope of interest of this work is the second order nonlinear term $\boldsymbol{P}^{(2)}(t) = \boldsymbol{\chi}^{(2)} \boldsymbol{E}^2(t)$, which is referred in literature as second order polarization and dictates three wave mixing nonlinear processes.

To derive rigorously nonlinear theory, one should solve Maxwell equations in medium. In vacuum where free charges are absent, Maxwell equations are reduced to the wave equation. Though in a medium this is no longer the case, the term $\nabla \cdot \mathrm{E}$ can still be neglected. In fact, it is identically zero assuming transverse plane wave, or small enough under *slow varying envelope* approximation (See Chap. 2 in Ref. [1]). Hence, wave equation remains valid in medium as well, only with an added material polarization term $\boldsymbol{P} = \boldsymbol{P}(t)$:

$$\nabla^2 \boldsymbol{E} - \frac{1}{c^2}\frac{\partial^2 \boldsymbol{E}}{\partial t^2} = \frac{1}{\epsilon_0 c^2}\frac{\partial^2 \boldsymbol{P}}{\partial t^2} \tag{1.3}$$

Now let's treat $\boldsymbol{P} = \boldsymbol{P}^{(1)} + \boldsymbol{P}^{NL}$ and $\boldsymbol{D} \equiv \epsilon_0 \boldsymbol{E} + \boldsymbol{P} = \boldsymbol{D}^{(1)} + \boldsymbol{P}^{(NL)}$. Assuming lossless, dispersion-less and isotropic material, we can write electric displacement field $\boldsymbol{D}^{(1)} = \epsilon_0 \epsilon^{(1)} \boldsymbol{E}$, where $\epsilon^{(1)}$ is frequency-independent dielectric tensor. In our case it's real scalar, but in general it does not necessarily have to be. Inserting the latter into equation (1.3) we get:

$$\nabla^2 \boldsymbol{E} - \frac{\epsilon^{(1)}}{c^2}\frac{\partial^2 \boldsymbol{E}}{\partial t^2} = \frac{1}{\epsilon_0 c^2}\frac{\partial^2 \boldsymbol{P}^{(NL)}}{\partial t^2} \tag{1.4}$$

Next, it's useful to perform frequency decomposition and solve for each component separately:

$$\begin{aligned} \boldsymbol{E}(\boldsymbol{r}, t) &= \sum_n \boldsymbol{E}_n(\boldsymbol{r}) e^{-i\omega_n t} \\ \boldsymbol{P}^{NL}(\boldsymbol{r}, t) &= \sum_n \boldsymbol{P}_n^{\boldsymbol{NL}}(\boldsymbol{r}) e^{-i\omega_n t} \end{aligned} \tag{1.5}$$

We can also lift up the frequency-independence condition of dielectric constant, so the general form would be $\boldsymbol{D}_n^{(1)}(\boldsymbol{r}) = \epsilon_0 \epsilon^{(1)}(\omega_n) \cdot \boldsymbol{E}_n(r)$. Inserting this with (1.5) into (1.3) we obtain nonlinear wave equation in frequency domain:

$$\nabla^2 \boldsymbol{E}_{\boldsymbol{n}}(\boldsymbol{r}) + \frac{\omega_n^2}{c^2}\boldsymbol{\epsilon}^{(1)}(\omega_n) \cdot \boldsymbol{E}_n(\boldsymbol{r}) = -\frac{\omega_n^2}{\epsilon_0 c^2}\boldsymbol{P}_n^{NL}(\boldsymbol{r}) \tag{1.6}$$

In order to solve the latter equation physical assumptions regarding to $\boldsymbol{P}_n^{NL}$ should be made. First, we expect the nonlinear term to be small, thus the solution to $\boldsymbol{E}_n$ will remain in form of plane wave (as in case of the homogeneous equation) except that the amplitude becomes a slow varying function of propagation coordinate z. Next, the reality of the fields and symmetry conditions considerably reduce the terms number in $\boldsymbol{P}_n^{NL}$ (1.6), since, nonlinear susceptibility is a tensor in general case (See Chap 1.5.3 in Ref. [1]). Next, as we will see in 1.2.2 when applying the Lorentz atom model to describe nonlinearity only the noncentrosymmetric media gives rise to the second term.

It's worth to give description of nonlinear phenomena on microscopic level, illustrated on Figure 1. Assume input field of two distinct frequencies ω_1 and ω_2 that excite nonlinear oscillating dipoles of

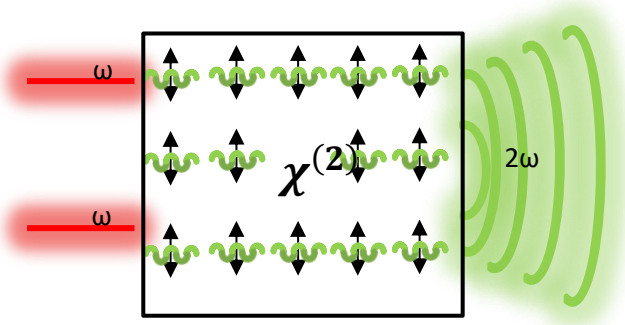

Figure 1 – Each of N atom in the material develops a double frequency oscillating dipole as a result of the nonlinear response to the applied field. If these dipoles oscillate in phase the radiated fields will be added constructively and the resulted SHG signal would be N times larger than a signal from a single atom.

frequency $\omega_1 + \omega_2$ in the sample. If these dipoles are in phase throughout the sample, they will be added constructively, producing sum frequency generated signal (SFG). Thus, in SFG process, phase matching rather than magnitude of second order susceptibility is determining factor in generating substantial nonlinear signal. For the field with wave vector k_3 resulting by product of mixing of the two input fields with wave vectors k_1, k_2, the phase mismatch parameter is defined by: $\Delta = k_1 + k_2 - k_3$ (See Figure 2). The resulting intensity of nonlinear field is proportional to: $I_3 \propto sinc^2(\Delta kL/\,2)$. Several phase matching techniques such as compensating by birefringent materials and Quasi Phase Matching (QPM) have been developed to reduce Δk. These techniques are out of the scope of the present work and can be found in Chap. 2 in Ref. [1].

A simple but trustworthy approach for $\chi^{(2)}$ order estimation is to recognize that when the applied field strength is of the order of an inner atomic field, the linear and the first nonlinear polarization correction term in equation (1.2) will be of the same magnitude. Hence, $\chi^{(2)} \cong \frac{\chi^{(1)}}{E_a(t)}$ where $E_a(t) = \frac{e}{\epsilon_0 4\pi\hbar^2 a_0^2}$ and a_0 is Bohr radius. Taking $\chi^{(1)} \approx 1$ which indeed a case and $a_0$to be Hydrogen atom radius we finally get $\chi^{(2)} \cong 1.94 \times 10^{-12}$.

1.2 Second Harmonic Generation

1.2.1 Energy consideration

In second harmonic generation (SHG) process two photons are absorbed by medium and one photon with a double frequency is emitted in parametric process. This process is depicted on Figure 2. Although, the solid line represents atomic ground sate, the dotted line levels are not energy eigenstates. They are referred as "virtual" levels, and are simply manifestation of energy conservation. It is noteworthy that the process as in Figure 2 is lossless. Electrons cannot populate an excited level or at most populate for brief interval of order of $\hbar/\,\delta E$ according to quantum-mechanical uncertainty principle, where δE is the energy difference between the ground and virtual states. This is due to excitation wavelength and thus virtual level is significantly detuned from the real atomic levels and no population transfer occurs, contrarily when virtual level coincides (or is close enough) with atomic level the electrons will be relocated to upper level, following by absorption of incident light. The process where initial and final energy states are identical earned the name "*parametric process*", while its counterpart is called nonparametric process.

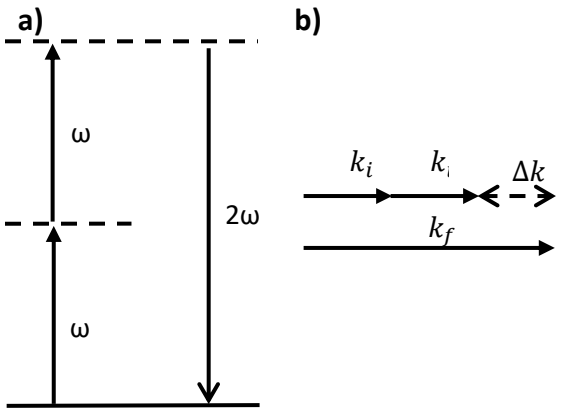

Figure 2 – a) SHG energy diagram: two photons are destroyed and one double energy photon is simultaneously created in lossless process. The dotted lines are not atom eigenstates but simply point on energy conservation b) Momentum mismatch diagram in 3 wave mixing process. On macroscopic scale even small momentum mismatch can dramatically reduce SHG effectiveness.

1.2.2 Second order susceptibility of classical anharmonic oscillator

In this section we will define second order susceptibility $\chi^{(2)}$ through the Lorentz atom model. In Lorentz model, an atom is threatened as harmonic oscillator. Despite being so simple, it gives good results

for linear susceptibilities of crystals, atomic vapors and nonmetallic solids. The shortcoming of harmonic oscillator model is that the atom has only one resonant frequency, which of course is not the case. The proper treatment of the problem is to take into account atom's energy eigenstates in scope of quantum mechanics. Nevertheless, since we restricted ourselves to sources operating in visible spectrum frequencies, which are much lower than the atomic resonance frequency the classical approach remains valid.

Assume the input field $(r,t) = Ee^{-i\omega t} + c.c.$. Applying this to nonlinear polarization given by (1.2) we get:

$$P^{(2)}(t) = 2\epsilon_0\chi^{(2)}EE^* + (\epsilon_0\chi^{(2)}E^2e^{-2i\omega t} + c.c.) \tag{1.7}$$

First term is time independent and called *Optical Rectification*, while the second term gives the field oscillating with frequency 2ω. We neglect the constant field amplification and focus only on the oscillating term.

Now, let's add a nonlinear term to electron's equation of motion in atom under external field $E(t)$.

$$\ddot{x} + 2\gamma\dot{x} + \omega_0^2 x + ax^2 = -eE(t)/m \tag{1.8}$$

Where ω_0 is an atom resonant frequency, γ is a damping coefficient and a is a strength of nonlinearity. The restoring force acting on electron according to (1.8) is:

$$F_{restore} = -m\omega_0^2 x - max^2 \tag{1.9}$$

This restoring force comes from the potential

$$U(x) = \frac{1}{2}m\omega_0^2 x^2 + \frac{1}{3}max^3 \tag{1.10}$$

The first term is a familiar harmonic potential and the second term is an anharmonic deviation term. Written in this form, the potential is suitable only for noncentrosymmetric media because of the odd powered distortion term. For centrosymmetric media, e.g. the potential build solely of even powers, thus

the first correction term will be of fourth order. The real potential compared to perfect harmonic potential is shown on Figure 3.

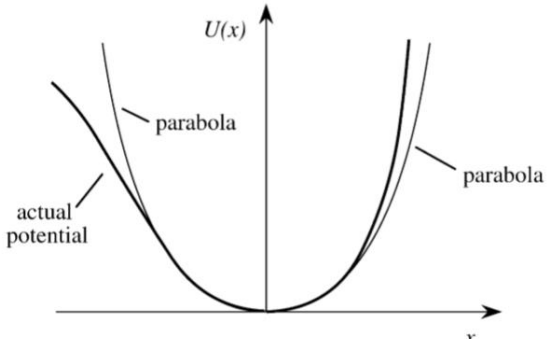

Figure 3 – Symmetric parabolic potential as function of electron displacement from equilibrium position and an actual noncentrosymmetric media potential containing small cubic term. Note that close to the equilibrium the deviation of actual potential from the parabola is small and can be treated as perturbation. The image is taken from Ref. [1].

The solution of Eq. (1.8) for plane wave field and with small nonlinear term ax^3 can be done by perturbation theory familiar from quantum mechanics. A solution in form of $x = \lambda x^{(1)} + \lambda^2 x^{(2)} + \lambda^3 x^{(3)} + \cdots$ is plugged into Eq. (1.8) and each $\lambda^i x^{(i)}$ satisfy the equation separately. The lowest order is a simply unperturbed harmonic equation with solution in form $x^{(1)}(t) = x^{(1)}(\omega)e^{-i\omega t} + x^{(1)}(\omega)e^{-i\omega t}$

$$x^{(1)}(\omega) = -\frac{e}{m}\frac{E}{D(\omega)} \tag{1.11}$$

Where$D(\omega) = \omega_0^2 - \omega^2 - 2i\omega\gamma$. With the help of latter, the first order correction term $x^{(2)}(t) = x^{(2)}(2\omega)e^{-2i\omega t}$, with amplitude $x^{(2)}(2\omega)$ given by:

$$x^{(2)}(2\omega) = \frac{-a(e/m)^2E^2}{D(2\omega)D^2(\omega)} \tag{1.12}$$

To derive susceptibility, two definitions of polarization are needed to be compared. In linear case these are $P^{(1)} = \epsilon_0\chi^{(1)}(\omega)E(\omega)$ and $P^{(1)} = -Nex^{(1)}(\omega)$. Hence, the linear susceptibility is

$$\chi^{(1)} = \frac{N(e^2/m)}{\epsilon_0 D(\omega)} \tag{1.13}$$

In the same manner for $P^{(2)}(2\omega) = \epsilon_0 \chi^{(2)}(2\omega) E^2(\omega)$ second order susceptibility is:

$$\chi^{(2)}(2\omega) = \frac{N(e^3/m^2)a}{\epsilon_0 D(2\omega) D^2(\omega)} \tag{1.14}$$

Applying (1.11) we can write (1.14) in different way

$$\chi^{(2)}(2\omega) = \frac{a\epsilon_0 m}{N^2 e^3} \chi^{(1)}(2\omega) \left(\chi^{(1)}(\omega)\right)^2 \tag{1.15}$$

1.2.3 Miller's rule

Examining the (1.15), one notice that the quantity $\frac{a\epsilon_0 m}{N^2 e^3}$ is roughly the same for all noncentrosymmetric crystals. Thus, the second ordered susceptibility, as well as $P^{(2)}(t)$ can be measured from the related first ordered quantities. This is called *Miller's rule* [2]. The coefficient of proportion $\delta = \frac{a\epsilon_0 m}{N^2 e^3}$ is known as *Miller's* delta and can be calculated, by assuming nonlinear and linear contribution the same when the electron distortion is on scale of an atom (as we did in *Nonlinear Optics Introduction* for $\chi^{(2)}$ estimation): utilizing atomic frequency $\omega_0 = 1 \times 10^{-16}\, rad/s$ with other physical constants yield $\chi^{(2)} \cong 10^{-12} m/V$.

Experimentally, Miller's rule found to be applicable for variety of materials even though the linear and nonlinear susceptibilities are spanned over four orders magnitude [3].

1.3 Nonlinear scattering theory approach for SHG

1.3.1 Metamaterials

The EM field-matter interaction, governed by Maxwell's equations, can be equally described on macro or microscopic level. On macroscopic level, material response is averaged over many atoms and routinely expressed via permittivity ϵ and permeability μ. The averaging is justified since the interatomic distance is much smaller than the electromagnetic field variation. For example, the field propagation in dielectric medium is described by refractive index $n = \sqrt{\epsilon\mu}$, so the effective speed of light is divided by n. The same effect can be also explained from an atomic perspective, namely by vector sum of the secondary

fields radiated as a response to the incident field, and propagating with the speed c. Obviously, changing materials microscopic properties will change the optical macroscopic behavior. This simple idea lays behind metamaterials, a novel class of structures, specially designed to possess some *"exotic"* optical properties. It's achieved by designing structures on subwavelength scale. The unit structure is several orders greater than atom's scale, but far less than the wavelength of interest, thus it's uniform from the EM field perspective (hence it is considered matter, not device). The word *"exotic"* usually refers to optical properties that are not observed in nature, though are not forbidden by Maxwell equations.

Materials can be classified by their ϵ and μ values as depicted on Figure 4. The vast amount of naturally found materials lie in a first two quadrants, whereas metamaterials are thoroughly designed to fall in to the lower quadrants. A striking example of these properties is negative index material (NIM). Consider the situation depicted in Figure 4, according to Snell law the incident and refracted angles are equal and opposite in direction, so refracted k vector propagates in opposite direction than the Poynting vector (note that no reflection occurs, since Fresnel reflection coefficient is zero). It can be proved that for both negative permittivity and permeability the refractive index is also have to be negative in order to observe causality [4]. In fact, E_r, H_r and k_r form left handed triplet, that's why NIM are often called "left handed" materials.

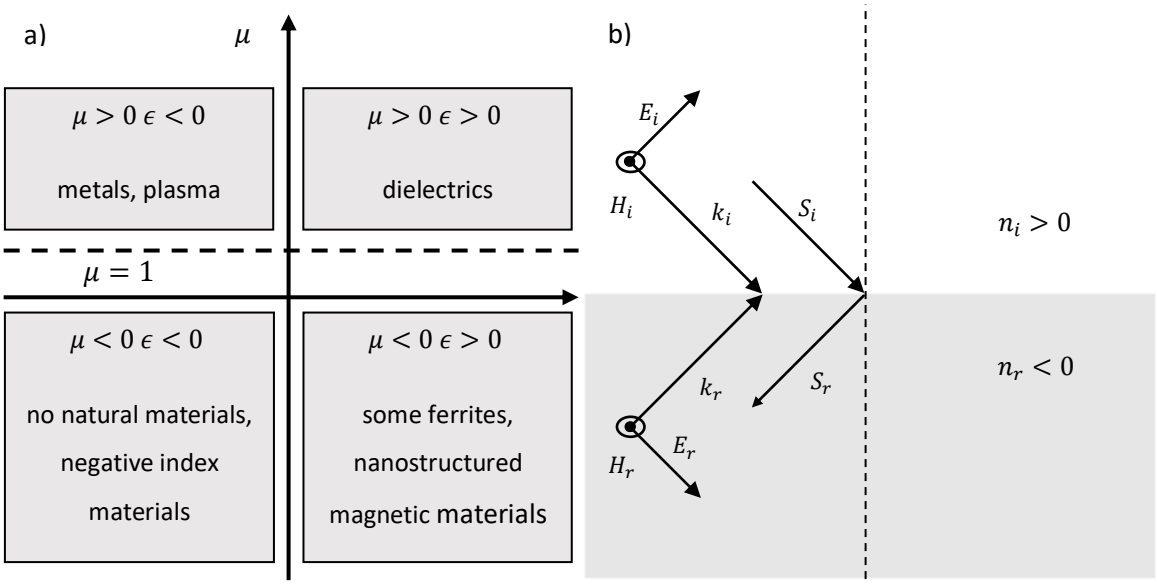

Figure 4 - a) Material parameter space characterized by electric permittivity ϵ and magnetic permeability μ. In optical wavelength most materials lie within thin line $\mu = 1$ b) Refraction at the interface between a positive and negative index material. The *k* and *S* vector are in abnormal opposite direction in the medium with negative refraction index.

While metamaterials linear response has been studied for a while with decent success, elaborated theory of nonlinear behavior is far from being complete. In the next chapter, we will focus on SRRs second harmonic generation.

1.3.2 Metamaterials SHG experiment

In a recent research work [5], O'Brien K. and Suchowski H. *et. al* questioned whether for metamaterials as well the Miller's rule remains valid in predicting second harmonic response from the linear one. To address this problem, they examined a 2D array with gradually changing asymmetry ratio from perfectly symmetric to high asymmetric split-ring resonator (**SRR**). The *Asymmetry (**AS**) Ratio* was defined as leg length over the total length of SRR and a total AS span of 0-0.3 was studied. Within the array, AS is gradually changing over X axis, while total length over Y axis. The 2D array is schematically illustrated on Figure 5.

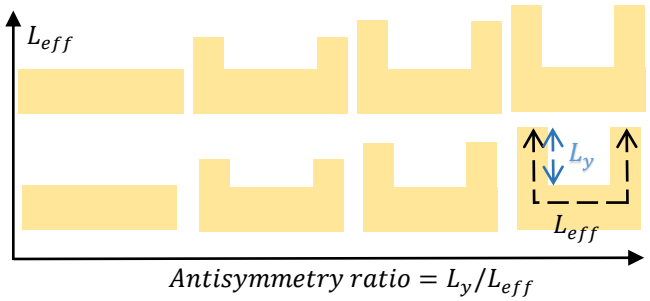

Figure 5 – Schematic of the examined SRRs array with varying asymmetry ratio and total length. The AS ratio is defined as leg length divided by the total nanostructure length and it is steadily increasing from left to right, e.g. in X axis direction, while total length is increasing in Y direction.

In order to examine exclusively intrinsic variations in nonlinearity, the total length L_{eff} remains unchanged within varying AS ratio, to avoid volume dependent changes. For the same purpose, the spacing between two adjacent SRRs was chosen big enough to prevent particle-particle interaction.

The array was excited by pump laser and the second harmonic signal is collected by confocal microscope in transmission mode. The Miller's rule predicted SHG response was calculated by observing transmitted field, since $\chi^{(2)} \propto \sigma^{(1)}(2\omega) \cdot \left(\sigma^{(1)}(\omega)\right)^2$, where σ is scattering cross section. The result is presented on the Figure 6 below:

While the measured optimal AS ratio for highest second harmonic signal was measured to be (~0.19), Miller's rule predicted smaller (~0.12). To resolve the discrepancy, the researchers suggested *nonlinear scattering theory* (**NLS**) approach which accurately predicted the right optimal AS ratio (See Figure 6).

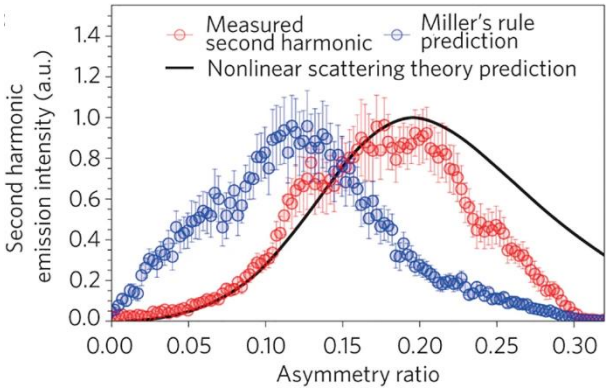

Figure 6- Experimental measurements of the SH emission for different asymmetry ratio geometries together with Miler's rule prediction calculated from transmission profile and nonlinear scattering theory numerical simulation. Miller's rule yields different result than the experiment, whereas NLS theory correctly matches the optimal geometry. The error bars indicate the standard deviation of the measured intensity. The image is taken from Ref. [5].

1.3.3 Nonlinear Scattering Theory

The nonlinear scattering theory (detailed in Ref. [6] and Supplementary Information in Ref. [5]) cornerstones are Lorentz reciprocity theorem and assumption that nonlinear properties can be described by surface susceptibility tensor.

According to Lorentz reciprocity, if there are two localized current sources j_1, j_2 which emit fields $E_1$and E_2 respectively, then their relationship is as follows

$$\int \boldsymbol{j}_2(\boldsymbol{r}', \omega) \cdot \boldsymbol{E}_1(\boldsymbol{r}', \omega) dV' = \int \boldsymbol{j}_1(\boldsymbol{r}, \omega) \cdot \boldsymbol{E}_2(\boldsymbol{r}, \omega) dV \tag{1.16}$$

Source j_1 is chosen to be ensemble of nonlinear dipoles on the surface of the nanostructure (See Figure 7)

$$j_1(\boldsymbol{r}, 2\omega) = \partial_t \boldsymbol{P}^{(NL)}(\boldsymbol{r}, 2\omega) = 2i\omega \boldsymbol{P}^{(NL)}(\boldsymbol{r}, 2\omega) \tag{1.17}$$

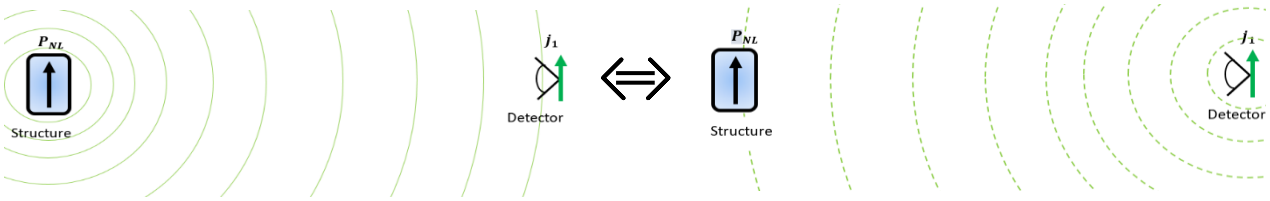

Figure 7 – The problem of finding the field radiated by ensemble of nonlinear dipoles on the structure surface is reduced to calculating overlap between the dipoles ensemble and the field radiated by test dipole placed on the detector.

We are interested in calculating the emitted field E_1 on the detector, therefore let's define j_2 to be current dipole of amplitude J_0 placed on the detector at $\boldsymbol{r_2}$

$$\boldsymbol{j}_2(\boldsymbol{r}, 2\omega) = J_0\delta(\boldsymbol{r} - \boldsymbol{r}_2)e^{-i2\omega t}\hat{\jmath} \tag{1.18}$$

Substitution of (1.18) with (1.17) into (1.16) yields to

$$E_1(\boldsymbol{r}_2, 2\omega) \cdot \hat{\jmath} = \frac{e^{-i2\omega t}}{J_0 \Delta l} \int 2i\omega \boldsymbol{P}^{(NL)} \cdot \boldsymbol{E}_2 dV \tag{1.19}$$

Where Δl is current dipole length. Equation (1.19) gives a field of frequency 2ω on the detector at $\boldsymbol{r}_2$. However, when using a numerical solver, it is often not convenient to calculate emitted field far away from the dipole. Instead, plane wave source approximation is used. As a result, the dipole's strength J_0 needs to be recalculated. It can be done by virtue of Green functions method (See Supplementary Information in Ref. [5]). For our purpose, i.e. finding agreement to the experimental results shown on Figure 6, the constant has little importance and a proportional relation can be used instead of equality.

Worth mentioning, that applying (1.19) to macroscopic 1D nonlinear crystal, the solution of both phase matching and absorption is in agreement with the direct solution of nonlinear wave equation [5].

The final step before the SH field from nanostructure can be calculated is to deduce $\boldsymbol{P}^{(NL)}$. Assuming the material is centrosymmetric, nonlinear contribution can arise only from structure's interface. We define a coordinate system with unit vectors $\hat{n}$ and $\hat{t_1}, \hat{t_2}$ to be normal and parallel to metal surface respectively. If the pump field is

$$\boldsymbol{E}(\omega) = E_n\hat{\boldsymbol{n}} + E_{t_1}\hat{\boldsymbol{t}_1} + E_{t_2}\hat{\boldsymbol{t}_2} \tag{1.20}$$

The nonlinear polarization is defined by nonlinear surface susceptibility 3rd rank tensor, with experimentally obtained components that are normal ($\hat{n}$) and parallel ($\hat{t}$) to the metal-air interface.

$$\boldsymbol{P}^{(NL)} = \chi^{(2)}_{nnn}\ E_nE_n\hat{\boldsymbol{n}} + \chi^{(2)}_{ntt}E_{t_1}E_{t_1}\hat{\boldsymbol{n}} + \chi^{(2)}_{ntt}E_{t_2}E_{t_2}\hat{\boldsymbol{n}} + \chi^{(2)}_{ttn}E_{t_1}E_n\hat{\boldsymbol{t}_1} + \chi^{(2)}_{ttn}E_{t_2}E_n\hat{\boldsymbol{t}_2} \tag{1.21}$$

This nonlinear polarization is timed by second harmonic field emitted by the source at detector

$$\boldsymbol{E}'(2\omega) = E'_n\hat{\boldsymbol{n}} + E'_{t_1}\hat{\boldsymbol{t}_1} + E'_{t_2}\hat{\boldsymbol{t}_2} \tag{1.22}$$

Substitution (1.20), (1.22) and (1.21) to equation (1.19), with the fact that the overlap integral is reduced to surface integral over nanostructure, yields to

$$E_{sh} \propto \int \boldsymbol{P}\cdot\boldsymbol{E}'ds \propto \int \chi^{(2)}_{nnn}E'_nE_nE_n + \chi^{(2)}_{ntt}E'_nE_{t_1}E_{t_1} + \chi^{(2)}_{ntt}E'_nE_{t_2}E_{t_2} + \chi^{(2)}_{ttn}E'_{t_1}E_{t_1}E_n + \chi^{(2)}_{ttn}E'_{t_2}E_{t_2}E_n dS \tag{1.23}$$

Exploiting (1.23) for calculating nonlinear signal for nanostructures depicted on Figure 8 both resonant and non-resonant conditions, K. O'Brien and H. Suchowski found that the major contribution come from χ_{nnn} component of susceptibility tensor

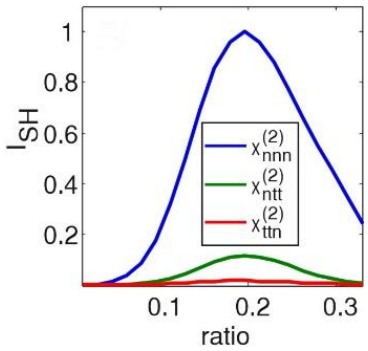

Figure 8 - SHG intensity as function of AS ratio for normal and tangential surface components of the local susceptibility tensor. The normal contribution is dominant, thus the two other donations can be neglected in the surface overlap integration.

Thus the final expression for overlap integral in (1.19) reduces simply to

$$E_{nl}(2\omega) \propto \iint \chi^{(2)}_{nnn} E_n^2(\omega) \cdot E_n(2\omega) dS \tag{1.24}$$

1.3.4 Microscopic dipoles overlap integral

Equation (1.24) states that in order to calculate second harmonic field one needs to sum contributions of nonlinear dipoles times the second harmonic field over the surface of nanostructure. These quantities are complex and have amplitude and phase. Therefore, to understand the experimental results on Figure 6 both amplitude and phase shall be assessed.

The amplitude of nonlinear dipole or polarization is determined by absorption cross section of the nanostructure. Thus, for the same effective length, the longest symmetric bar will produce higher amplitude dipole. On the other hand, larger asymmetry donates to better interference between nonlinear modes. Clearly, the optimum overlap is a compromise between structure length and asymmetry ratio for given effective length. The latter concept is illustrated on following Figure 9 from Ref. [5]. The blue bar has the greatest amplitude but its overlap is highly destructive. On the other hand, despite the green structure's modes are perfectly in phase due to the highest asymmetry, the amplitude of each mode is not that high, so isn't the net emission. Alternatively, the intermediate structure strikes a balance between amplitude and nonlinear microscopic sources interference that yields to the optimal second harmonic signal.

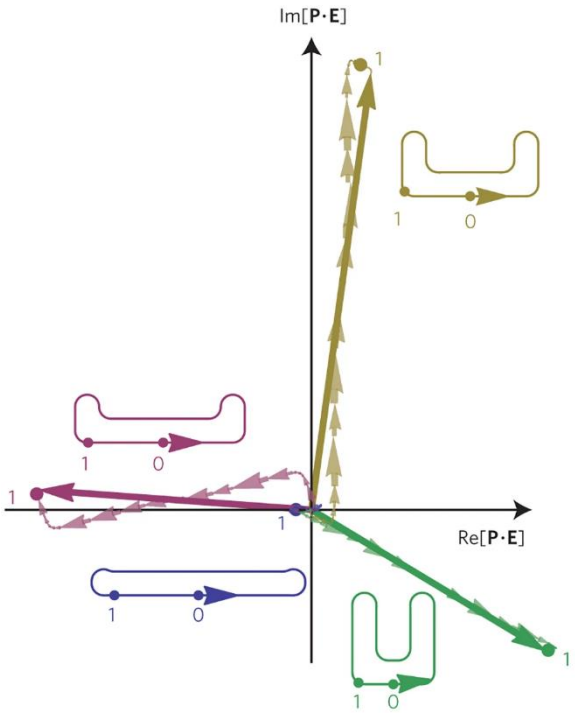

Figure 9 - $P \cdot E$ plotted on complex plane along the path around the nanostructure for various dimension of the nonlinear structures. As can be seen, for straight nanobar, local sources cancel each other. Alternatively, while the most asymmetric green structure has a best sources interference, the overall signal is not the highest, due to the lower sources amplitude. The optimal signal is generated by intermediate asymmetry yellow structure, compromising amplitude and dipole phases. Image is taken from Ref. [5].

To summarize, nonlinear scattering theory correctly predicts optimal asymmetry ratio for second harmonic signal and gives physically intuitive explanation of net nonlinear emission.

2. SNOM microscopy

2.1 Resolution limit in optical microscopy

As was previously mentioned in 1.3.4, the straight bars have a local nonlinear response. Nevertheless, in accordance to nonlinear scattering theory, its overall contribution is annihilated by destructive interference of local SH sources. Thus according to this theory, one is supposed to observe strong SH optical signal just over the surface of the bar, compared to zero or close to it in the farfield. The so called nearfield imaging is derived from *Super-resolution imaging*, which is of considerable importance in vast areas of science and industry.

According to Rayleigh criterion for the diffraction limit, two images are just resolvable when the maximum of diffraction pattern of one object is directly over the minimum of the diffraction pattern of the other, see Figure 10. For objective with circular aperture the resolvable distance between two separated points is

$$\Delta x_{min} = 1.22\frac{\lambda}{NA} \tag{2.1}$$

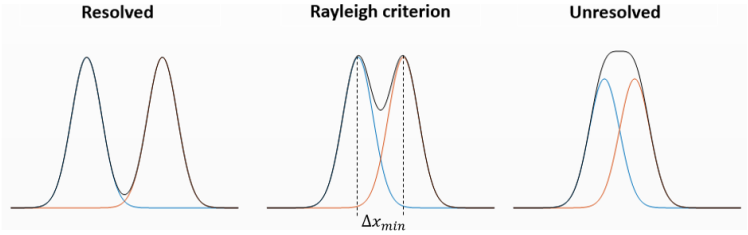

Figure 10 – Rayleigh resolution criterion states that the minimum separation of two resolvable point sources is when the first diffraction minimum of the Airy disk of one image coincides with the maximum of the second point.

Where *numerical aperture* is defined by $NA = nsin(2\theta_{max})$, with *n* is a refractive index and $2\theta_{max}$ – the maximum collection angle of the optical system. Modern microscopes have NA within range 0.95 – 1.4, achieving spatial resolution $\Delta x_{min} \cong \lambda/2$, which is 200-400 nm for visible light. A demand for nanoscale imaging lead to development of variety of microscopic techniques. In the following chapter,

briefly explained *scanning nearfield optical microscopy* (SNOM), which allows investigate dielectric properties of the sample.

2.2 Working principle of SNOM

2.2.1 AFM microscopy

SNOM (also referred as NSOM - nearfield scanning optical microscopy) is built atop atomic force microscopy (AFM). AFM uses a sharp tip to scan a topography of a sample surface. The schematic illustration of an apparatus is depicted on Figure 11. The sharp tip is moved across the sample at very small distance. There are both attractive and repulsing forces acting on the tip as a function of distance from the sample's surface. The main attraction force comes from Van der Waals forces, furthermore, potential difference can lead to Coulomb attraction. The repulsive forces mostly are governed by ionic and Pauli repulsion. When tip gets closer to the sample the repulsive forces dominate, bending the cantilever to the opposite direction. Similarly, if the distance from the sample attractive forces overtake, the cantilever bends downwards. The cantilever bending is sensed by reflected laser from the cantilever's backside and analyzed by position sensitive four segment photodiode.

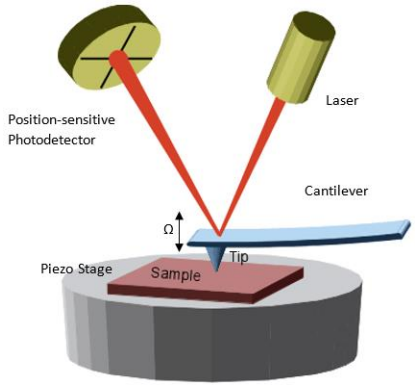

Figure 11 - Work scheme of AFM microscope operational mode. Image taken from Univ. of Santa Barbara.

There are two operational modes in AFM. In the contact mode, the position of deflected laser is kept constant, while the feedback system varies tip-sample distance through elevating or lowering Piezo stage. The output of the feedback is translated to the topographical map of the sample. Differently, in the tapping mode the cantilever with the mounted tip is oscillating in tip's resonant frequency (typically within

10-300 kHz range). The interaction forces, described previously, are responsible for the amplitude damping. By demodulation the signal of the position-sensitive photodiode, the oscillation amplitude can be monitored with high precision. A feedback system keeps the amplitude constant by varying tip-surface distance, in similar matter as in contact mode. The tapping mode is particular useful for SNOM as will be discussed later.

AFM reaches vertical resolution ~1 angstrom and the lateral resolution ~ 10 nm which is in scale of tip's apex. This high resolution with lack of requirement on vacuum chamber and no constraint on sample preparation compare to SEM earned AFM esteem in research community and its inventors Binning G. and Rohrer H. won Nobel Prize in 1986 just few years after its introduction.

2.2.2 Tip Illumination

Since the development of AFM, various techniques were introduced to extend AFM beyond simple height measurement. An example of these kinds of efforts is aperture SNOM, which utilizes tapered optical fibers as probing tips, aimed to achieve nano-optical imaging. The sample is illuminated through the tip's aperture providing a nanoscale resolution, simultaneously with the AFM mapping. The downside of this technique is low light transmission through the aperture just several tens of nanometers in width making it barely impractical, particularly for infrared part of the EM spectrum. To overcome this constraint an apertureless SNOM was introduced. In apertureless SNOM metal or metal-coated AFM tips are illuminated with focused laser beam. A metal like tip acts like antenna concentrating charges at the tip apex. The "*lightning rod*" effect known from electrostatics together with Surface Plasmon Polariton (SPP) gives rise to an enhanced local field, confined to apex tip with is much less than wavelength [7]. When the illuminated tip gets close enough to the surface, the nanoscale enhanced field interacts with the sample. This nearfield interaction modifies the scattered field from the sample. The scattered light is collected with the same parabolic mirror that focus the beam on the tip and then measured with a detector (Figure 12 (a)). On the Figure 12 (b) depicted the numerical simulation of field at the tip illuminated by plane wave

with linear polarization perpendicular to the tip's surface. The local field enhancement is clearly seen to be confined to the size of the tip and falling exponentially with the distance.

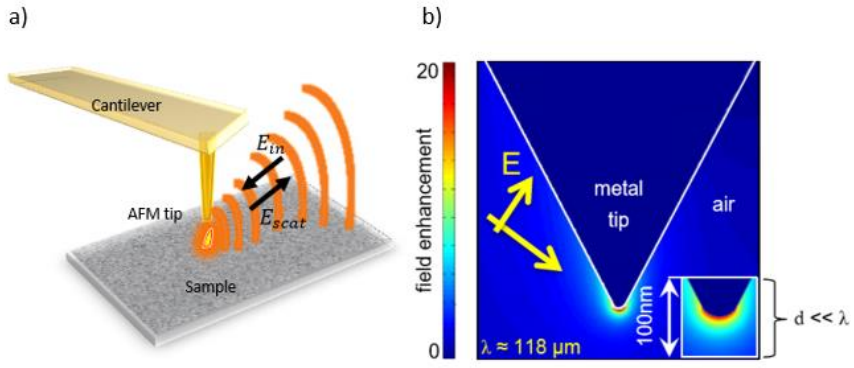

Figure 12 - a) A sharp AFM tip iluminated by focused laser beam scatters interaction field b) Numerical simulation of a metal cone, illuminated by farfield light with λ=118µm (taken from Ref. [14]).

The tip-surface interaction through strong evanescent field can be calculated from applied radiation by complex scattering coefficient σ_{scat} which relates applied E_{in} and scattered E_{scat} fields.

$$E_{scat} = \sigma_{scat} E_{in} \tag{2.2}$$

Due to the strong localization of interaction field, the σ_{scat} and thus recorded backscattered light carry information about local sample properties in a scale of size of the tip. Hence SNOM microscopy deliver nanoscale resolution on order of $\approx 10nm$ [8].

In addition to nanoscale resolution there is another benefit in extracting a nearfield. In the wave front $U(x, y, z)$propagating in the space (Figure 13) not all discrete spatial frequencies will reach point *d* in the farfield.

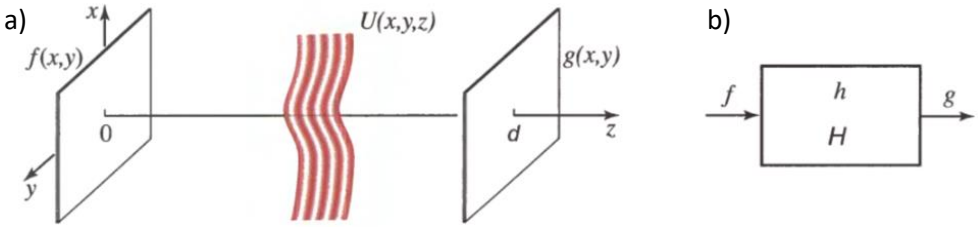

Figure 13 – a) Propagation of the light wavefront *U(x,y,z)* a distance *d* between two planes *f* and *g* in free space b) This propagation can be expressed by transfer function *h* with associated Fourier transform *H*. Image is taken from Ref. [13].

Inspecting the transfer function given by

$$H(\nu_x, \nu_y) = \exp\left(-j2\pi d\sqrt{\lambda^{-2} - \nu_x^2 - \nu_y^2}\right) \tag{2.3}$$

We see that for frequencies higher than $\nu_{max} = |\lambda^{-2}|$ the propagating field falls exponentially and is not observable in farfield. These high frequencies contain data about the sample, hence collecting evanescent field for imaging benefits of extra sample information that is not available in standard imaging practice.

2.2.3 Background noise suppression

Considering the laser source in near IR spectrum (λ ~ 1μm) the spot size even for the diffraction limited case would be on order of half of micron. Clearly, in that case only the tiny part of backscattered light contains tip-sample nearfield interaction, while the majority is undesirable scattering from the sample background, cantilever and shaft. The detector measures intensity I_{det}, as a result, for field $E_{sca} = E_{nf} + E_{bg}$ the signal output will be mixed by unavoidable background contribution

$$I_{det} \propto I_{sca} \propto \left|E_{nf} + E_{bg}\right|^2 = \left(E_{nf} + E_{bg}\right)\left(E_{nf} + E_{bg}\right)^* \tag{2.4}$$

As mentioned in 2.2.1 SNOM is built on AFM operating in tapping mode, with the tip is oscillating vertically with frequency Ω. Owing to the tip oscillation, the scattered field is demodulated by Ω and E_{sca} now can be written as

$$E_{sca} = E_{nf} + E_{bg} + \sum_{n=0}^{\infty} E_{nf,n}\cos(n\Omega t) + \sum_{n=0}^{\infty} E_{bg,n}\cos(n\Omega t) \tag{2.5}$$

Where $E_{nf,n} = \sigma_{nf,n}E_{in} = s_{nf,n}e^{i\phi_{nf,n}}E_{in}$ and $E_{bg,n} = \sigma_{bg,n}E_{in} = s_{bg,n}e^{i\phi_{bg,n}}E_{in}$ are the nearfield and background scattering fields Fourier components of the n^{th} order. The AFM taping amplitude is set to be far below the applied beam focus radius. Due to the taping mode the gap between tip and sample varies sinusoidal. The evanescent interaction field is sharply nonlinear with tip-surface distance. Contrarily background scattering either not sensitive to modulation at all or has at most linear dependence. Therefore, by demodulating the detected signal to higher harmonics $n\Omega$ (usually $n \geq 2$)

nearfield scattering coefficients $\sigma_{bg,n}$ are sufficiently filtered from negligible $\sigma_{bg,n}$ [9]. Having said that, the resolved signal would still comprise background contribution of $E_{bg,0}$ as a result of mixing of harmonic coefficients. For order n≥2 the measured intensity is

$$I_{sca} \propto |E_{sca}|^2 = E_{bg,0}E^*_{nf,n} + E^*_{bg,0}E_{nf,n} \tag{2.6}$$

This is known as multiplicative background. An approach called *Pseudo heterodyne detection* allowing to measure completely background free nearfield signal can be found in Ref. [10].

It was mentioned that for background filtering the taping amplitude is chosen to be far below the wavelength. However, the amplitude by no means can be automatically raised with shifting incoming beam spectrum deeper in infrared region. Otherwise, in the upright position the scattering would be solely from the tip with no sample interaction portion. The typical values for tapping amplitude is ~30-100 nm.

2.3 Theory of SNOM

A theoretical treatment to associate the measurable quantity σ_{scat} (see formula 2.2) to samples physical property based on scattering theory from a realistic elongated metallic tip can be very tedious. In this chapter presented the approach of much more simplified geometry, with the tip is modeled by dipole sphere placed on the tip apex and the sample is modeled by simple plane. This dipole model can be found in Ref. [8] and [11], additionally, see [8] for the extension of current simple dipole to more accurate finite dipole model. The dipole model is presented on Figure 14. The tip is modeled by a sphere

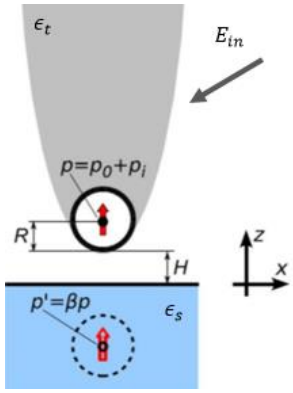

Figure 14 - SNOM dipole model. The incident field E_{in} induces dipole *p* on metallic AFM tip that is modeled by a sphere of radius *R* placed in a distance *H* from the sample with dielectric function ϵ_s. The nearfield tip-sample interaction is described by mirror dipole *p'* on the sample. Image from Ref. [8].

of radius *R* placed on the tip's apex in a distance *H* from the sample – a semi-infinite plane characterized by dielectric function ϵ_s.

Tip polarization by incident electric field can be modeled by dipole sitting in the sphere center. Due to the p-polarization of incoming field and the tip elongation, the polarized dipole $p_0$is assumed to be oriented along the tip axis, e.g. in *z* direction. The dipole can be related to incoming field by polarizability

$$p_0 = \alpha E_{in} \tag{2.7}$$

Within a scope of electrostatic approximation (see Ref. [12]) the polarizability (in air) can be calculated by

$$\alpha = 4\pi R^3 \frac{\epsilon_t - 1}{\epsilon_t + 2} \tag{2.8}$$

This dipole polarizes the sample, inducing a mirror dipole

$$p' = \beta p_0 \tag{2.9}$$

Where $\beta = (\epsilon_s - 1)/(\epsilon_s + 1)$ called surface response function. The mirror dipole acts back on the tip, increasing its polarization. The stronger tip dipole strength the mirror dipole which polarizes further tip dipole and so forth. Thus the total mirror dipole can be written as

$$p' = \beta(p_0 + p_i) \tag{2.10}$$

Where p_i is an interaction induced part of mirror dipole p'. We can introduce a dimensionless tip-sample interaction distance function *f* to rewrite $p_i = fp'$ and together with (2.10) result in

$$p_i = f\beta(p_0 + p_i) \tag{2.11}$$

Defining $g \triangleq f\beta$ the total dipole $p = p_0 + p_i$ is

$$p = \frac{p_0}{1-g} \tag{2.12}$$

The electric field induced by mirror dipole on tip and separated from the mirror dipole by distance $D = 2(R+H)$ (see Figure 14) is given by

$$E = \frac{p'}{2\pi D^3} \tag{2.13}$$

The field is responsible for the induced dipole moment $p_i = \alpha E$ on tip. Substituting this dipole moment together with definition of *f* function into (2.13) leads to

$$f = \frac{p_i}{p'} = \frac{\alpha}{2\pi D^3} \tag{2.14}$$

Finally, we apply distance *D* and $g = \beta f = \frac{\beta\alpha}{16\pi(R+H)^3}$ to get expression for the total dipole polarized on the tip

$$p = E_{in}\frac{\alpha}{1-\frac{\alpha\beta}{16\pi(R+H)^3}} \tag{2.15}$$

It's suggested to define effective polarizability from the last expression

$$\alpha_{eff} = \frac{\alpha}{1-\frac{\alpha\beta}{16\pi(R+H)^3}} \tag{2.16}$$

Where $\beta = \beta(\epsilon_s)$. Recalling that the nearfield scattering coefficient σ_{scat} defined as ratio of scattered light from the tip to incident illumination $(\sigma_{scat} = E_{scat}/E_{in})$ is proportional to tip dipole model *p*, we immediately deduce that $\alpha_{eff} \propto \sigma_{nf} = s_{nf}e^{i\phi_{nf}}$. Bearing in mind that the tip oscillates with frequency Ω the effective polarizability time course becomes $\alpha_{eff} = \alpha_{eff}(h(t))$, with $h(t) = A(1+\cos(\Omega t))$. Utilizing the Fourier theorem, we straightforward deduce that spectral components obey the proportionality as well

$$s_{nf,n} \propto |\alpha_{eff,n}|$$
$$\phi_{nf,n} = \arg(\alpha_{eff,n}) \tag{2.17}$$

3. Study of nearfield nonlinear optical fields

In this section, I will elaborate on the numerical and experimental efforts toward a study of nonlinear optical generation in the near-field optical regime. I will start by developing the numerical framework of nonlinear scattering theory, which was used to study the nonlinear response various metamaterials geometries.

3.1 Numerical Simulation

3.1.1 Simulation environment

The purpose of numerical simulation part was to reproduce the simulation result of the work [5]. While their work was implemented with COMSOL Multiphysics® finite element solver, we carried our work in finite-element Lumerical FDTD solver. The SRR geometry was constructed out of the rectangular blocks. The total 500×500×2500 nm domain was simulated. The plane wave was injected at normal incidence and the scattered field was recorded separately in proximity of the structure and close to domain wall extracting the near and farfield respectively. The perfect matched layer (PML) boundary conditions (BC) were set in the transverse plane (*Z*-direction) and periodic BC were set in in the *XY* plane. The simulated gold nanostructures length spanned from 240 to 352 nm with 4 nm step and the asymmetry ratio for every length changed gradually from 0 to 0.3, while the width was kept constant of 40 nm. The nanoparticle was placed atop of SiO2 (glass) host resembling a real sample as is shown on Figure 15.

The plane wave source is chosen to be linearly polarized along the nanostructure axis to promote particle absorption and scattering, demanded for effective polarization. The wavelength span over 500 – 1500 nm. Such a wide range is aimed for retrieving both fundamental and doubled frequency scattered fields from a single simulation. Yet, Lumerical solver always injects broadband pulse (with regard to requested wave range) rather than the plane waves. Nevertheless, the scattered field is normalized by the Fourier transform of the signal $s(t)$, therefore the fields are “amplitude variations free” and use of single simulation for both fundamental and SH field is still valid.

The glass and definitely the air do not absorb light in simulated wavelength range in contrast to gold. This property was exploited to estimate the normal-to-surface scattered field, required for an overlap integral calculation as formula (1.24) suggests. In further details, the spatial mask was built so that it is equal to one in an area where the imaginary part of the refractive index changes from zero to nonzero value and zero everywhere else, e.g. it is nonzero only on boundary between the gold and dielectric materials. The recorded scattered field was multiplied by this mask, living solely the surface field. In total, three masks for coordinates *X, Y and Z* were introduced to obtain the normal to surface fields. Finally, the fields of excitation and second harmonic wavelength were multiplied and integrated in accordance to (1.24).

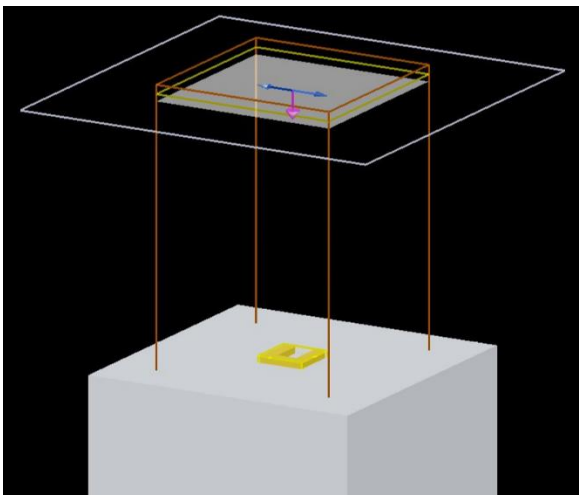

Figure 15 – Nano-particle simulation environment. SRR particle made of gold sits atop of the glass host. The linearly polarized light field is injected from the top at normal incidence and the polarization is parallel to particle's base. The image is from Lumerical™ simulation.

3.1.2 Miller rule prediction

First, Miller second harmonic prediction was evaluated. As was mentioned in section. 1.3.2 the linear susceptibility is proportional to extinction cross section. The cross section was estimated by taking log of transmission at resonance and SH wavelengths in consequence of Beer-Lambert law: $A_\lambda \propto l\sigma_{ext}$, where *l* is a light path length, σ_{ext} is an extinction cross section and A_λ is the absorbance at given wavelength, defined as:$A_\lambda = -log\mathrm{T}$, where T is referred as transmittance.

On Figure 16 is plotted second harmonic signal averaged among structures with different lengths as function of asymmetry ratio. It can be seen than the optimal as ratio is 0.16 ± 0.07 while the Ref [5]

implies 0.12 ± 0.02. The distortion is anticipated, since the reference's calculation was built upon transmission experimental data rather than pure numerical simulation. Secondly, the particle geometry in the presented simulation was straight in contrast to the rounded corners in the cited research.

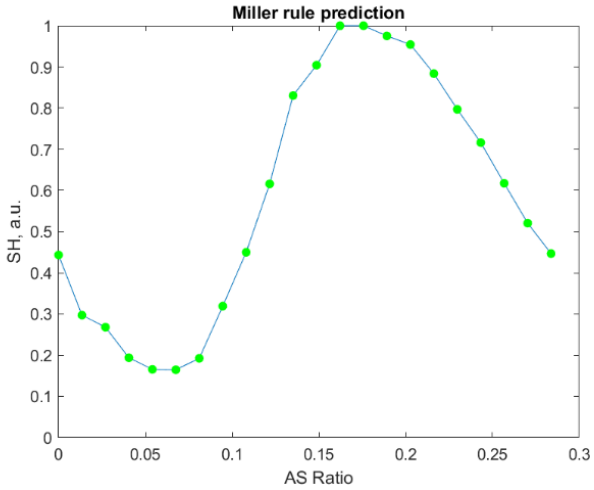

Figure 16 – Second harmonic intensity as a function of asymmetry ratio following by Miler rule prediction. The result was normalized. As can be seen the optimal ratio is about ≈0.16, slightly different from the result obtained by [5], which is anticipated due to the change in the simulated geometry and different numerical solver used. The negative slope for the low asymmetry rate is due to the numerical sensitivity to the geometry change.

To get intuitive idea behind Miller rule the transmission profile for three split ring resonators with the same length but different asymmetry ratio is depicted on Figure 17. The resonant frequency together with its half-wavelength companion is marked by star symbol. As the curvature of particle increases the absorption cross-section becomes smaller so the transmission is higher, on the other hand, the higher AS ratio promotes formation of second resonance mode. According to (1.24) the Miller' susceptibility is built out of the product of this two contributions, therefore some intermediate geometry yields the largest nonlinear response.

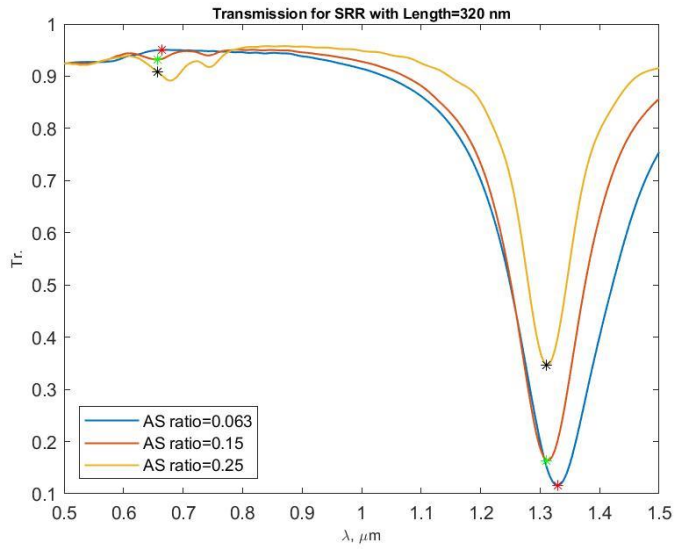

Figure 17 – Second harmonic intensity as a function of asymmetry ratio following by Miler rule prediction for particles with low, mild and high asymmetry as explained by graph legend. The result is normalized.

As can be seen from the Figure 17 the absorption frequency shows only slight shift with an asymmetry change. The optimal SH resonance wavelength independence was confirmed experimentally by Ref [5] and is consistent with our assessment (see Figure 18). Nonetheless, the geometry change does have an effect, notably in short wavelength regime. Therefore, the slight change in resolving the fields or transmission at resonant wavelength would be exacerbated at half wavelength. We assume that this

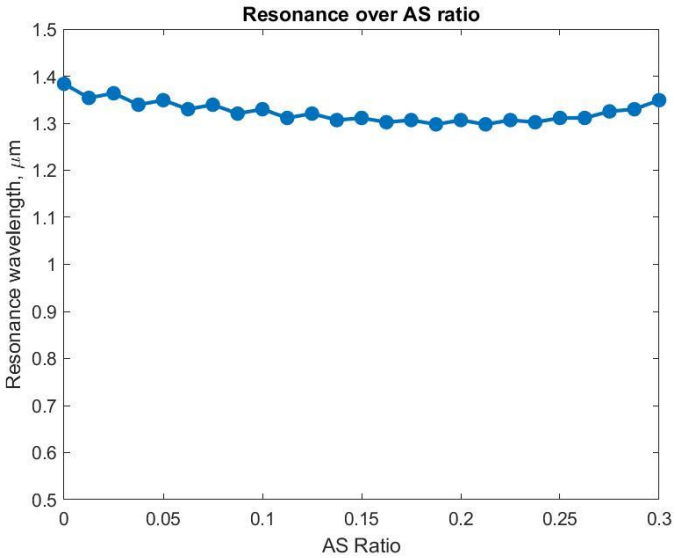

Figure 18 – Resonance wavelength dependence on as ratio for 320 nm long SRR nanostructure. The resonance wavelength is roughly the same for equivalent length structures with the asymmetry ratio varying from 0 to 0.3. The result is compliant to the findings from Ref. [5].

vulnerability is responsible for negative slope in low AS ratio part of Figure 16, as well of deviation from the bell curve. Refining the simulation parameters and decreasing the simulation mesh size had little improvement. The geometry related numerical errors are more prominent in overlap integral calculation and will be discussed further in this chapter.

3.1.3 Overlap integral calculation by Nonlinear Scattering model

The nonlinear scattering theory simulation result represented on Figure 19 is evaluated at fundamental wavelength ≈1100 nm, e.g. below the resonance. The founded optimal ratio is 0.2 ± 0.01, e.g. shifted to higher AS ratio with respect to Miller's rule result as anticipated. Examining other wavelengths effect exhibit only slight distortion as far as the wavelength is not close enough to the resonance and "second mode region". Concerning SH calculation on resonance, some numerical instabilities issue impaired the results. I found that the simulation environment was very sensitive to geometry change. In numerical solver perspective the most numerically "vulnerable" part is a boundary between two materials with different dielectric properties (in our case it is gold particle with air or glass) and the surface overlap integration only exacerbated the situation, since all but metal surface fields were ignored in the calculation. Decreasing the solver's mesh size did not change the situation greatly.

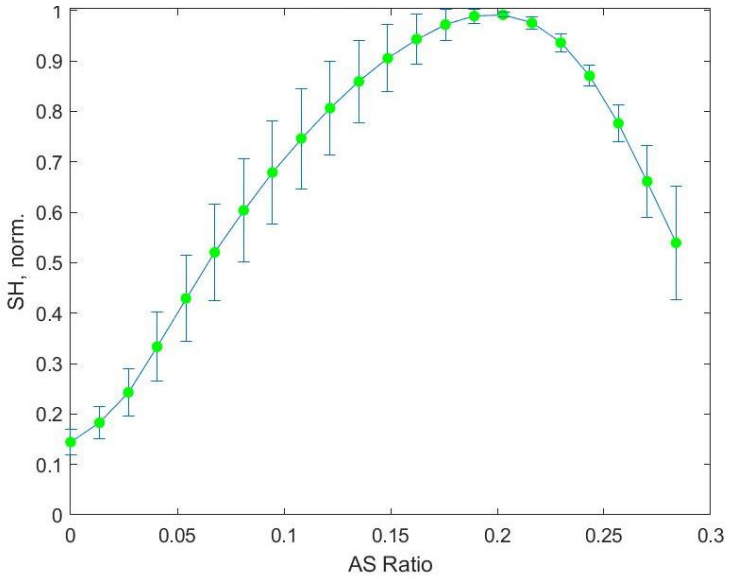

Figure 19 - Normalized second harmonic signal VS asymmetry ratio at 110 nm excitation light wavelength. The signal is averaged over particles with length ranging from 240 to 352 nm.

It is clear from the discussion in 3.1.2 that Miller's rule is only suitable for on-resonance (or close to it) prediction, while nonlinear scattering theory is capable of forecasting an optimal geometry for a wide

range of light spectrum (certainly after solving the on-resonance instability issue). This fact reveals a second advantage of nonlinear scattering theory comparing to Miler's rule, besides more accurate results in nanoscale regime.

To grasp an intuition behind the "bell" curve, on Figure 20 we plotted second harmonic signal strength and phase angle for three particles with low, intermediate and high asymmetry. Looking over column Figure 20*(a)* one can recognize that particle 1 has slightly better signal with less dark spots than highly asymmetric particle 3, though the overall particle 3 signal is two times higher as it seen in Figure 20*(c)*. Since a total SH signal is calculated by summing all complex valued dipoles over particle's perimeter, the directions between the points in complex plane play a central role in overall result. Examining the phase angle plots in *(b)* one can notice the phase positive and negatives segments. These segments can be divided into pairs, each pair consisting of two segments with similar length and opposite phase in order to cancel one another. For example, SRR with 0.14 AS ratio has three pairs, one vertical and two horizontal -"bright" and "pale". There are no sections that left unpaired and hence, particle 1 total nonlinear signal is somewhat low. On the other side, particle 3 legs inner sides are in-phase (both blue) so cannot be paired and hence contribute to the total sum. Therefore the highest signal originates from intermediate geometry 2, which is compromise between field strength and in-phase sections (I suppose that for geometries with round corners the trade-off between amplitude and phase will be more emphasized due to strong signal amplification on corners, which is obviously unphysical).

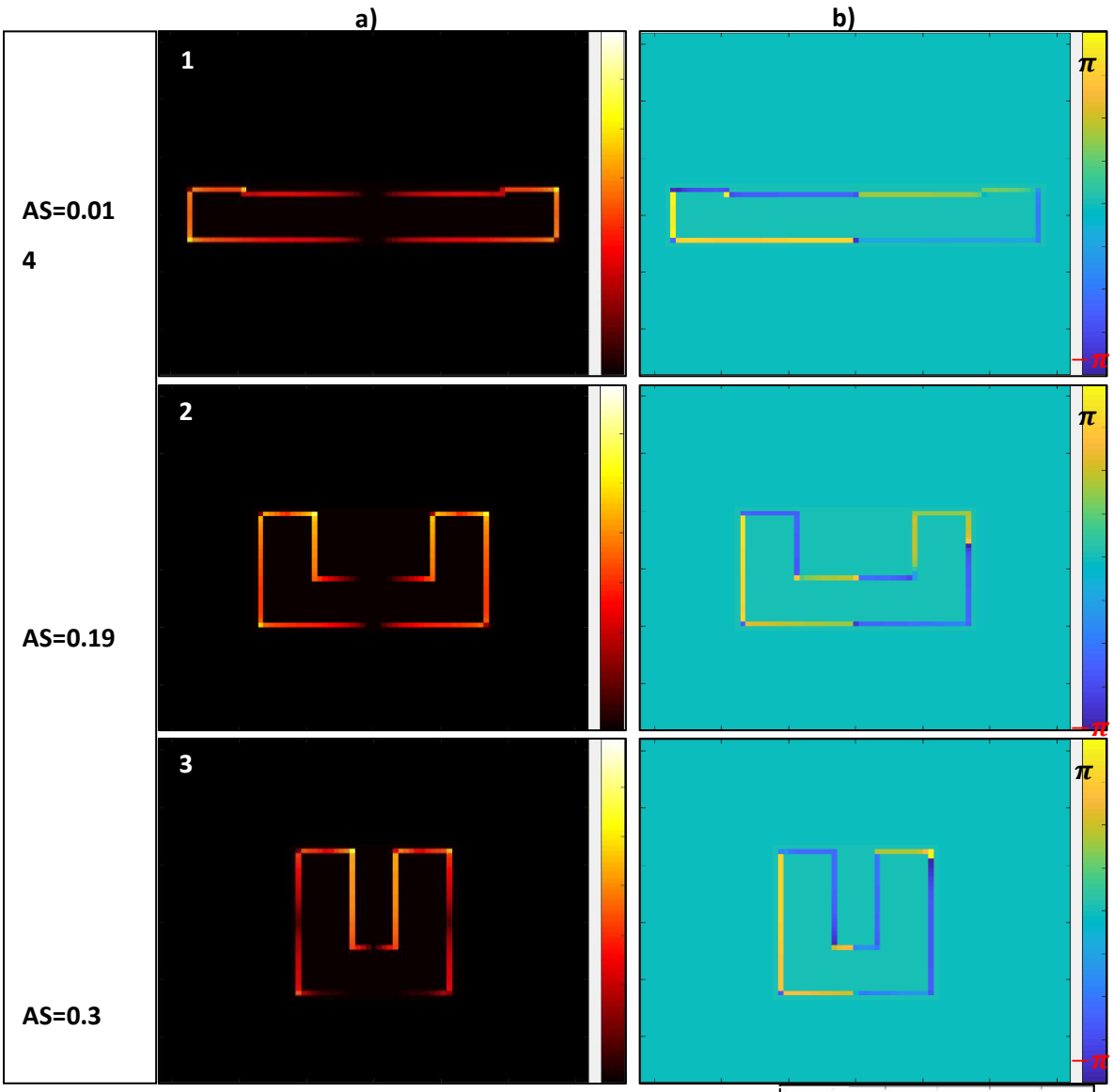

Figure 20 - a), b) The absolute SH field with complementary phase angles of nonlinear dipoles distribution on SRR perimeter for three different structures with light, mild and strong asymmetry. The all three structures are 280 nm length and the calculation is based upon one slice at excitation field of 1100nm. Actual field scale is logarithmic to improve structure-to-background contrast for better visibility.

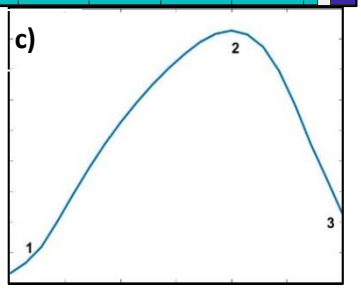

c) SH signal over AS ratio profile for selected structures length.

This result is in line with the findings shown in Ref. [5] cited in 1.3.4, that a second harmonic signal is compromise between absorption at fundamental and second harmonic and the sources ability to combine constructively.

3.1.4 SHG prediction in various geometries and general conclusion

To test further the complex phase and amplitude interplay in overall SHG, the nonlinear scattering theory was applied to the particles with other geometries that are still close to SRR.

The S-type structure was made out of SRR by rotating the right leg 180° with respect to particle base (See pictogram on Figure 21). The simulation result of second harmonic response over different asymmetry ratios is plotted on Figure 21, with the optimal AS ratio is 0.186, close to the SRRs result (0.2).

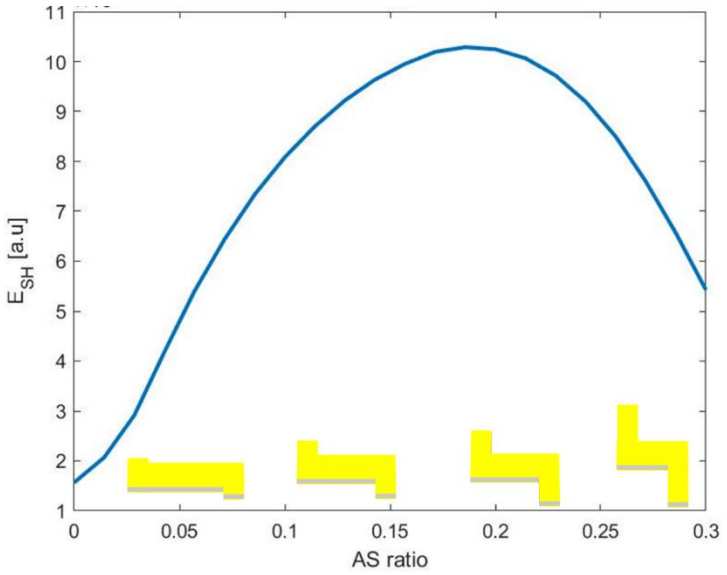

Figure 21 - Second harmonic signal plotted as function of asymmetry ratio for S-type particles, which are identical to SRRs except the right leg is flipped over the particle longitudinal axis. The structures geometry transformation is schematically illustrated on the lower part of the figure close to X-axis. The optimal geometry has asymmetry ratio of 0.186 with the total length fixed at 280 nm and the fundamental wavelength was set to 1100 nm as for SRR.

We proceed in the same manner as in par. 3.1.3, namely plot the second harmonic amplitude and phase distribution along the structure for 3 particles with low, mild and high asymmetry on the Figure 22.

It can be seen from the right side of the Figure 22 that the most asymmetric structure has the most in-phase local nonlinear dipoles. However its amplitude is lower than the mild asymmetry structure as it looks slightly dimmer than the nanoparticle with AS ratio 0.19. The most symmetric structure has the most segments out of phase that cancel one another and its signal is also lower. Thus, the finest signal is resulted from mild asymmetry particle having both good local dipoles signal strength and overall vector sum.

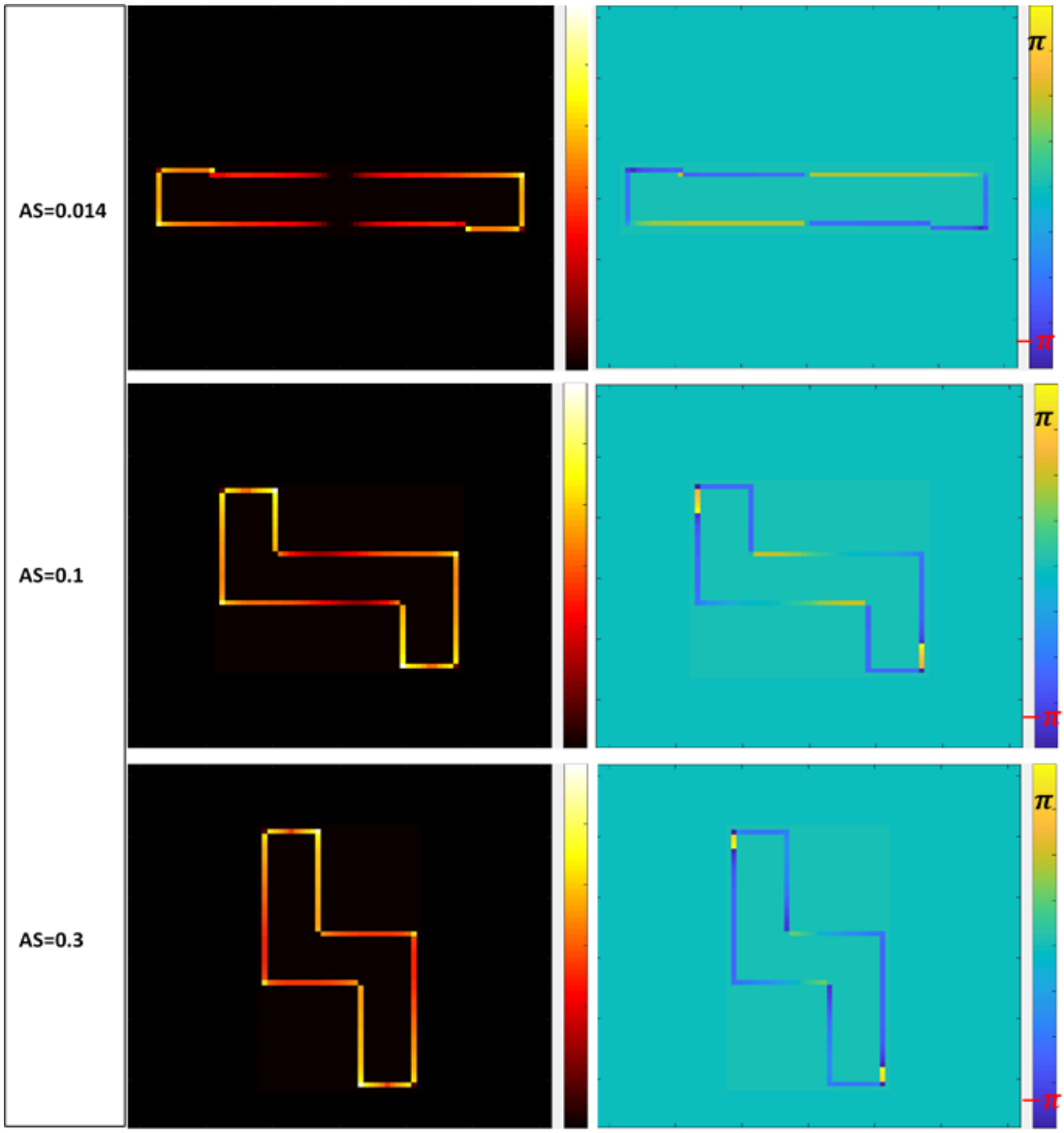

Figure 22 – Distribution of SHG signal amplitude in the left column and complex phase in the right column, along the perimeter for 3 S-types structures with low (AS=0.014), mild (AS=0.19) and high (AS=0.3) asymmetry. Each point on the structure represents the local dipole contribution to SHG calculated according to NLS theory. The total nonlinear signal depends on both the amplitude of the nonlinear dipoles and their ability to constructively summing up, i.e. being in phase.

Another simulated geometry is L-type structures, the particle consisting of one leg that is twice longer with respect to SRR or S-type to avoid SHG volume dependence. The signal-AS ratio dependence is depicted on Figure 23. The maximum second harmonic signal is generated by the structure with asymmetry ratio of 0.11, this noticeable "bell" curve shift to the low asymmetry region for L-type geometries can be explained by further symmetry braking with respect to the lateral axis. And again, to grasp intuition behind the curve, we proceed by plotting the amplitude and the complex phase distribution along the 3 different AS ratio structures on Figure 24.

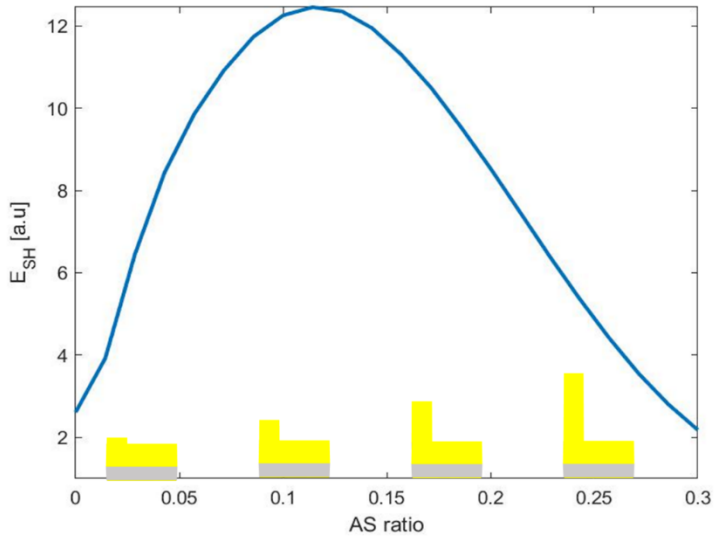

Figure 23 – NLS prediction of second harmonic signal as function of asymmetry ratio for L-type particles. The particles changing geometry schematically plotted along X-axis. As for S-type the total length was held constant at 280 nm and the excitation wavelength is 1100 nm. The maximum SHG is produced by nanoparticle with AS ratio equal to 0.11.

Starting with the complex phase pattern we see at most destructive interference occurs in the lowest asymmetry ratio particle. Regarding the mild and high asymmetry, the variation between them is not so prominent, most of their nonlinear dipoles are in phase for both of the structures. Despite the big difference in the phase profile, the overall signal between the least and the most asymmetric structures are of the same order. This is due to the lower dipoles amplitudes along the structure with AS ratio 0.3, as it appears generally dimmer than the other two structures. The "black spot" in the most symmetric particle contains out of phase segments, so the final result is not affected that much. As anticipated, the

highest nonlinear response is generated by mid asymmetry particle with both fair dipoles amplitude and their ability to sum constructively on complex plane.

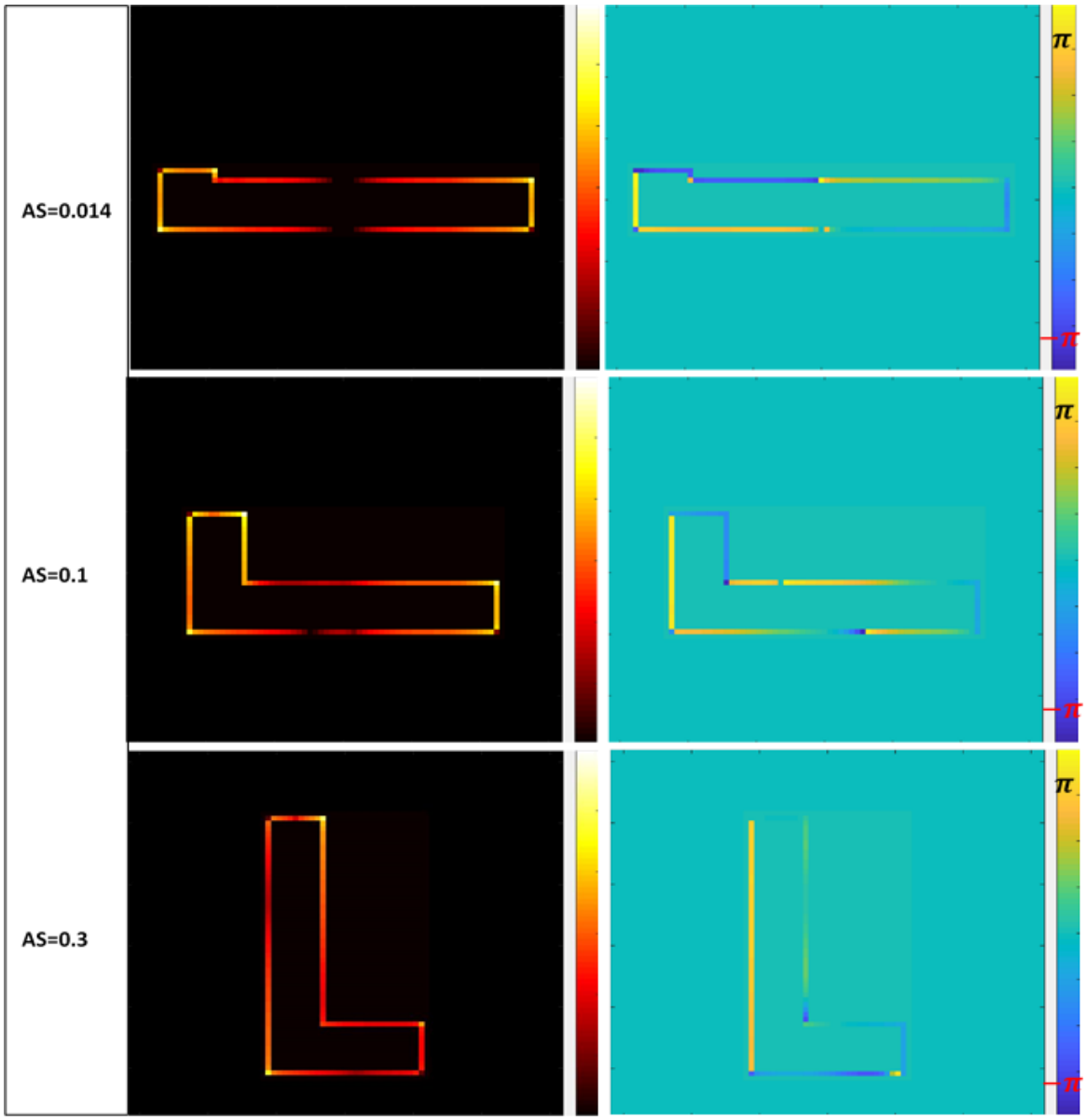

Figure 24 - Distribution of SHG signal amplitude to the right and complex phase to the left, along the perimeter for 3 L-type nanoparticles with low (AS=0.014), mild (AS=0.1) and high (AS=0.3) asymmetry. Each point on the structure represents the local dipole contribution to SHG calculated with respect to NLS theory. All structures, e.g. SRRs, S-type and L-type are plotted with the same color scale limits.

While we have showed that the particles geometry has a strong effect on complex phase and amplitude distribution, there is a question that still needs to be answered: "Do they contribute equally or one of the contributions is more significant than other in total second harmonic signal"? To tackle this question we sum just the amplitudes of local dipoles, e.g. eliminating the phase and compare the result to complex sum prescribed by NLS theory (See Figure 25).

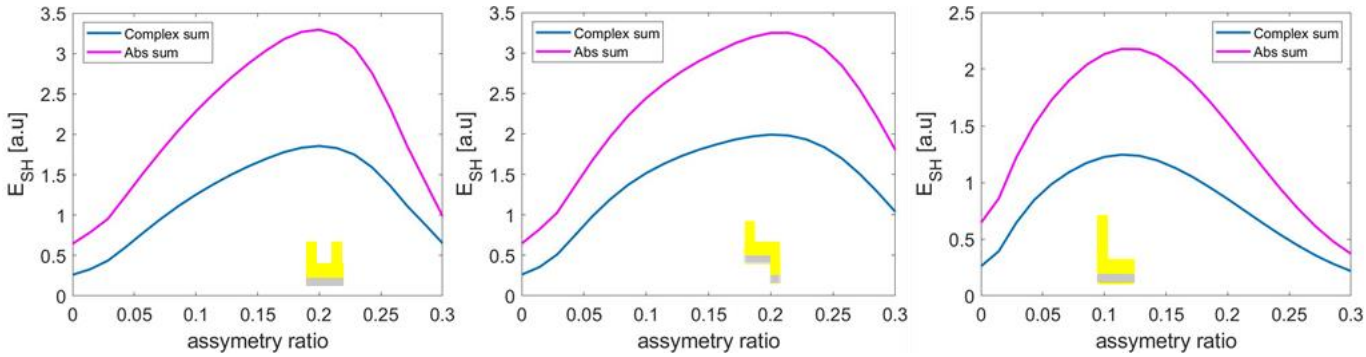

Figure 25 – Second harmonic signal as function of asymmetry ratio calculated first by NLS theory, e.g. by summing the dipoles in complex plane (blue) and the calculation based on the scalar sum of dipoles amplitude (purple) for SRR, S-type and L-type structures. The pictogram of each particle is placed on the appropriate graph below the optimal asymmetry ratio. Excluding the complex phase from the SHG calculation has a very minor effect on best AS ratio location, rather on the signal amplification.

Surprisingly, turning to the scalar summation had a little effect on the peak position for all structure types. The peak shift to lower AS ratio, compared to NLS theory prescribed vector sum of complex values along the nanoparticle, would indicate on lack of destructive interference due to phase ''switch off" (See the AS=0.014 particles on Figure 20, Figure 22 and Figure 24 and the related discussion). However, excluding the phase from the calculation didn't improve SHG for particles with mostly out of phase pairs that cancel each other, but led to the signal amplification in all simulated geometries with variance in both asymmetry and the structure types. We suppose that this kind of behavior can occur when there is strong signal amplification on the structures corners, so just the few points on the particle's surface are the major contributors to nonlinear signal, and the phase between these few high signal points is responsible for the lower signal in complex compare to the absolute values summation. Regarding a cancelation effect of summing complex vectors over the whole particle's surface, while existing it is actually overwhelmed by these few "strong players".

In future work, this assumption can be examined by simulating the structures with rounded geometry in order to eliminate the field amplification on sharp edges. Besides these edges are unphysical, the rounded geometry will also help to investigate if the numerical instabilities discussed in par. 3.1.3 are indeed geometry related.

3.1.5 Supplementary tests

Since the peak position is not changing either we sum complex or scalar values, several other tests could be done to further explore nonlinear optical properties of nanoparticles. First we can ask which out of the 3 types SRR, S-type or L-type gives best second harmonic response. The result is presented on Figure 26. Clearly, the S-type is an optimal choice with SRR signal is only slightly lower for all asymmetry ratios.

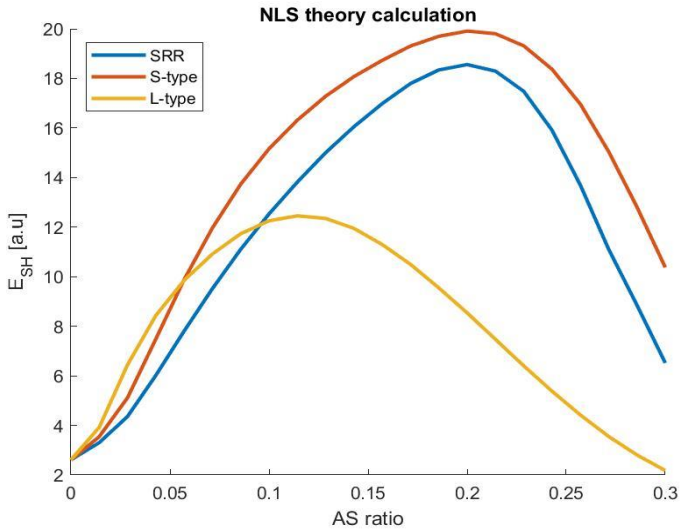

Figure 26 – Comparison of SHG produced by SRR, S-type and L-type as function of asymmetry ratio plotted on the same Y axis scale plot. All the simulated structures have total length of 280 nm and the calculation was performed for pump wavelength equal to 1100 nm.

Recalling that for SRRs Miler's prediction returned lower optimal AS ratio than the nonlinear scattering theory (see par. 3.1.3), the same comparison can be performed for the other 2 particle types. It is clearly seen from the results presented on Figure 27 that Miller's rule disagreement with NLS theory is not exclusive to SRR geometry.

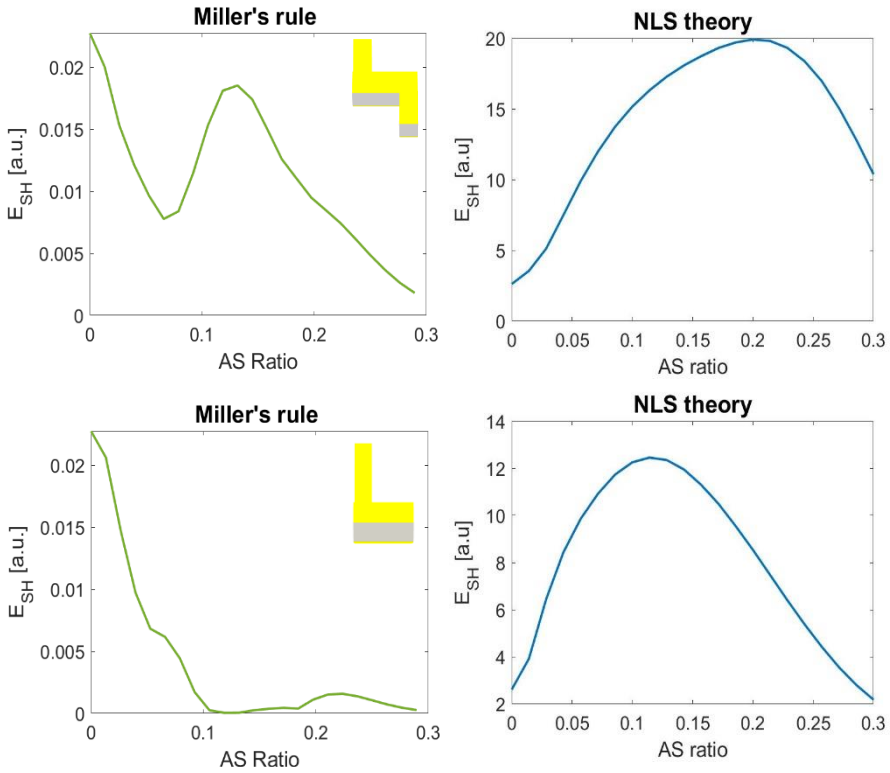

Figure 27 - Miller's rule estimation compared to the nonlinear scattering theory SHG calculation for S-type structures in upper and L-type structures in lower figure's part. Similar to split ring resonators the Miller's rule prediction is not matched to NLS theory. For both structure types the length is set at 280 nm and the fundamental wavelength in NLS calculation is 1100 nm.

Next we can examine particle width influence on second harmonic response. While the all previous simulations were executed with constant width of 40 nm (See par 3.1.1), in this test the particle's length and AS ratio are kept constant at 280 nm and 0.2 respectively and the particle's width is gradually increased from 34 to 48 nm with step of 4 nm. The lower width limit was set to ensure that the resonance is within the selected wavelength range and the upper width is limited by particle's legs overlap. To minimize the SHG frequency dependent changes, the calculation was done for fundamental wavelength that is further shifted from the resonance, e.g. is in the upper limit of the simulated pump wavelength that is equal to 1000 nm. Since particles cross section in transverse plane is a square, the width parameter also determines the height of the structure. Hence to distinguish between different dimensions contribution, the SHG overlap integral was calculated separately over single slice and over the whole surface of the nanoparticle. The results is presented on Figure 28 (*a*). The linear and parabolic graph shapes suggests the simple perimeter or area scaling. However these contours are not exact line or parabola due to the width dependent resonance shift that introduces frequency related variations in second harmonic response (See Figure 28 (*b*)).

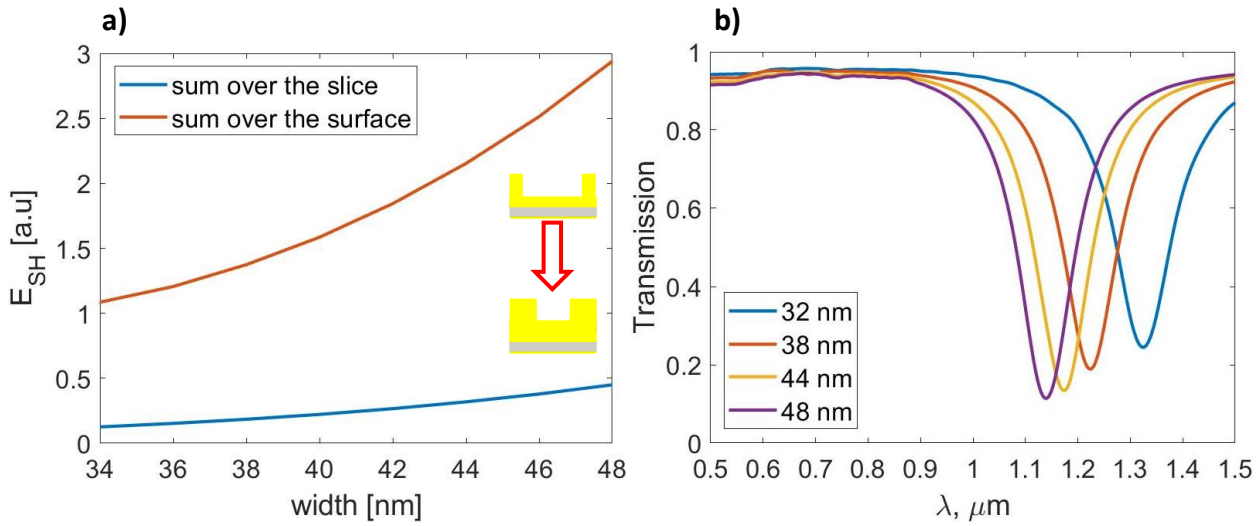

Figure 28 - a) SHG dependence on particle width calculated in two ways: once over a single slice in a plane normal to Z-axis (blue) and once over the whole particle surface (red). The linear and parabolic graphs shape point on their respective perimeter and area scaling. The schematic increase in the width is illustrated on the right side of the figure b) Transmission profile for different particle's width. The pump wavelength was set to 1000 nm to minimize frequency related changes in nonlinear response.

Furthermore it is worth to test SHG dependence on polarization angle. Recall that the previous simulations were performed with linearly polarized plane wave parallel to the nanostructure base. Introducing the field rotation in XY pane leads to the drop in nonlinear response as it can be seen on Figure 29. The reason for that is the fundamental mode sharp fall with the increase of polarization angle, also note the simultaneous rise of secondary mode. This mode is associated with the field component that is parallel to the nanoparticle's legs.

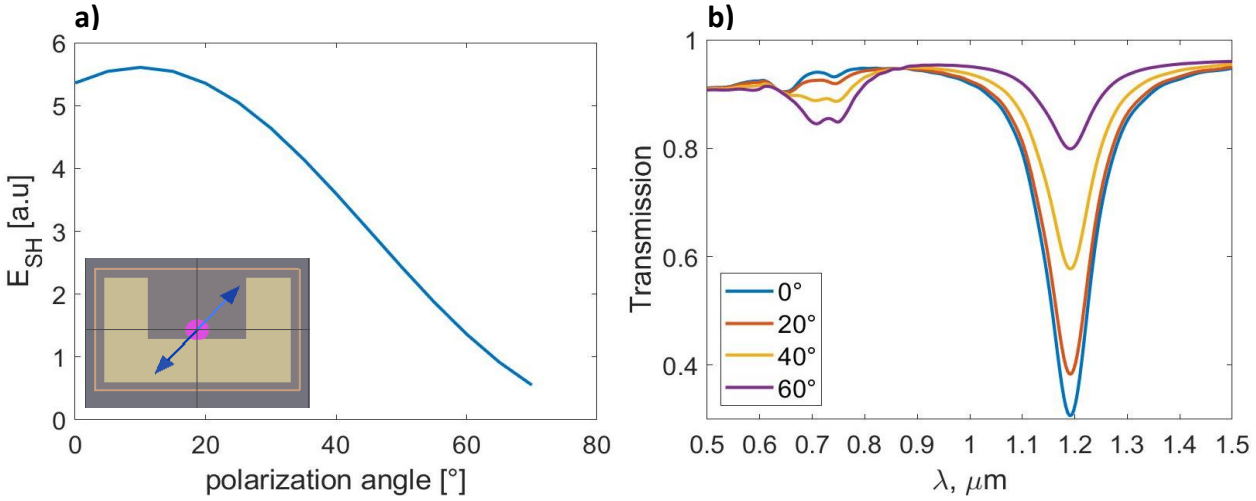

Figure 29 – a) Second harmonic signal as function of polarization angle, where 0° refers to the pump field parallel to the base of nanoparticle. The illustration of the field direction with respect to the structure is illustrated at the left lower corner of the figure and the image is taken from Lumerical™ simulation environment b) Optical power transmission profile for a different polarization angles. First fundamental mode falls gradually with the angle increasing, although, grows the secondary mode related to the legs parallel EM field component.

To summarize the discussion above, in nanoparticles design for nonlinear optical respond beyond the asymmetry ratio, there are various parameters to be taken into account.

3.2 Experimental results

3.2.1 Sample characterization

In order to investigate SHG strength from nanostructures surface, the sample constituting of different geometries was fabricated. Prior to fabrication, the numerical simulation was run in order to define optimal geometry for maximum absorption within 1000-1200 nm wavelength range. According to (1.19) the highest SH signal is achieved through the maximum material polarization (absorption resonance), which is linked to the structure's length. Thus, the preferable illuminating wavelength should match the nanostructure geometry and vice versa.

Uri Arieli and Omri Meron prepared the fabrication using Electron Beam Lithography technique. The sample constitutes of blocks of nanostructures with the same geometry. Refer to Figure 30 for schematic array illustration. The nanostructures, made of gold with a thickness of 40 nm, are rest on SiO substrate. The thin layer ~ 20 Å of indium tin oxide (ITO) is applied to enhance gold to silica adhesion. For each blocks row in *X* direction the legs length remains constant, while the base gradually increases moving from left to right from 120 to 200 nm. Similarly, when sliding in *Y* direction, the blocks base length is kept unchanged whereas legs length are growing from 0 to 60 nm. The particles are spaced 500 nm apart and the adjacent

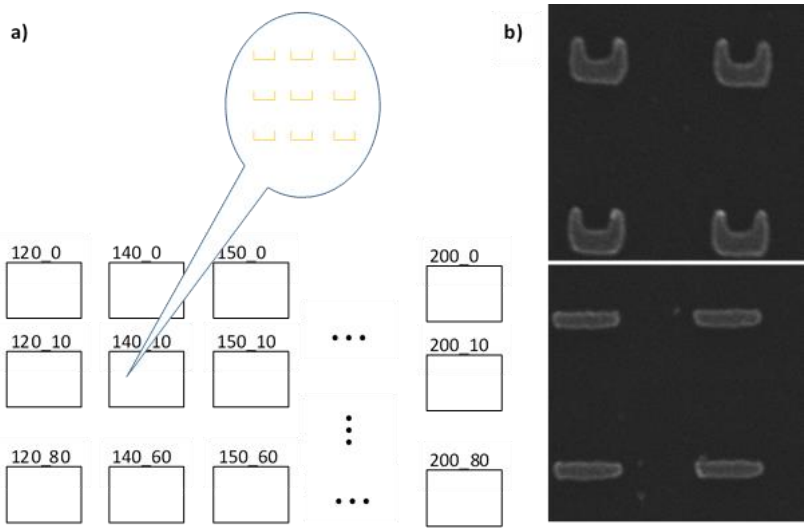

Figure 30 –a) Scheme of nanostructures array. Each block is built of metamaterials with identical geometry. Structures asymmetry varies gradually in Y direction, and the base length is changing in X direction b) The SEM image of two types of particle: SRRs in the upper and bars in the lower image respectively (the sample fabricated by Uri Arieli and Omri Meron).

rows are separated 800 nm to avoid coupling between the nanoparticle, giving the investigated AS ratio spanned from 0 to 0.29.

Prior to SNOM scanning, the sample's absorption spectrum was examined (See Figure 31) . In addition to finding absorption resonance, the second harmonic response in far-field of different structures was validated with regard to Ref. [5]. Both of these tests were executed with the help of custom built microscope by Uri Arieli for his research.

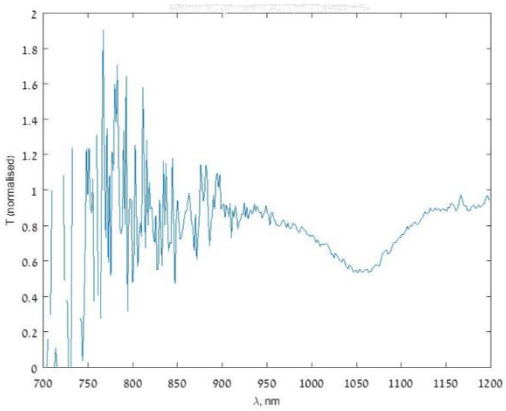

Figure 31 - SRR has absorption resonance at ≈1070 nm. To enhance SHG process, the nanostructures were chosen to have a resonance close to the fundamental wave of 1080 nm.

In absorption spectrum test, the sample was illuminated by broadband (400 – 1300 nm) OSL2 fiber illuminator light source from Thorlabs™ and the spectrum was resolved with the help of Yokogawa™ AQ6370D spectrum analyzer with wavelength range of 600 to 1700nm and wavelength resolution 0.02nm. The obtained transmission spectrum was normalized to the spectrum of plain SIO substrate. The example of transmission with absorption peak around 1025 nm can be seen on the figure below. The spikes in low frequencies are a consequences of optical fiber lack of uniformity for visible spectrum wavelength range.

3.2.2 Experimental setup

The experimental setup is shown on Figure 32. The sample was illuminated with 100 fs, 80 MHz repetition rate pulse beam, linearly polarized in normal direction, manufactured by Spectra-Physics Mai-Tai™ laser. The short pulse together with high repetition rate delivers a large amount of energy to the sample, maximizing second harmonic generation as (1.23) suggests, whereas the time between pulses ensures heat dissipation, preventing the sample destruction. The peak intensity was centered near 1086 nm in agreement with SRR's absorption resonance in Near-IR range. Passing thorough SNOM microscope

(neaSNOM from Neaspec™), the light is focused by parabolic mirror on tip, stimulating the tip-sample contact. The same parabolic mirror collects scattered field from the tip and reflects it back to the beam splitter which redirect it to photomultiplier detector. Since the peak is centered at ~1080 nm, we expect the second harmonic signal to be in green part of wavelength spectrum. To avoid green light leakage to detector from the source and the lab environment, at first prior to target illuminating, the input light beam is filtered by longpass filter, expelling short wavelength waves. Second, the collected light is passed through narrow band-pass filter, retaining only 543 nm wave.

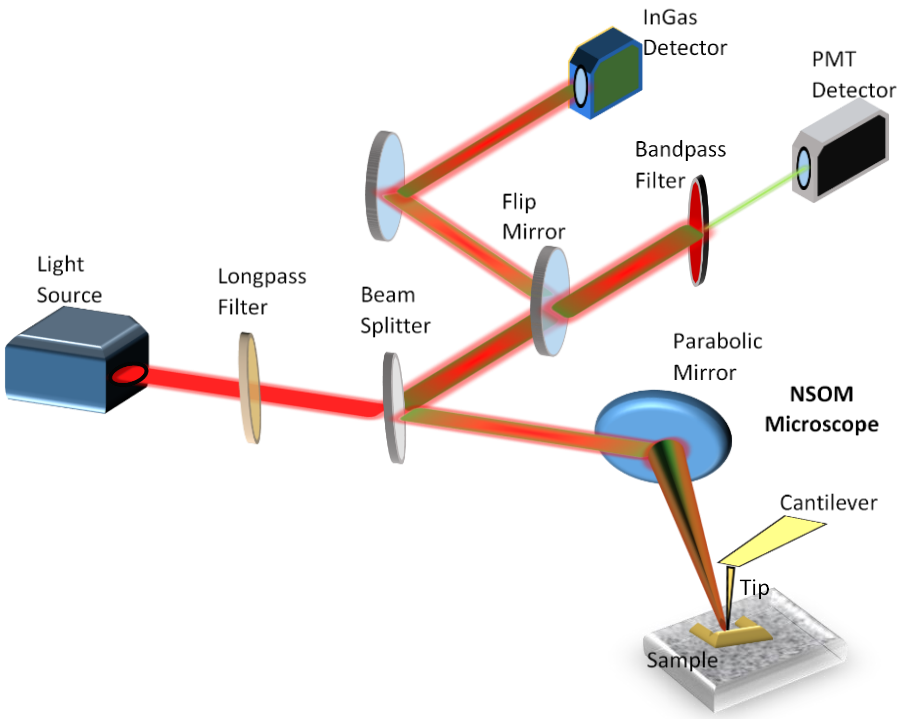

Figure 32 – Nearfield SHG experimental setup. The 1080 nm laser pulse beam is filtered and focused through the parabolic mirror on the SNOM tip. The generated SH signal is collected with the same parabolic mirror, reflected back to the beam splitter and after filtering through the narrow band ≈543 nm filter is detected by the high sensitive PMT detector. Additional flip mirror takes unfiltered signal to near IR detector in order to facilitate the tuning the optical system to collect the most of the reflection from SNOM.

It is straightforward that the second harmonic intensity is very sensitive to tip-sample interaction strength. Inaccuracy in beam focusing, beam collimation, damaged AFM tip, SNOM parabolic mirror position and other settings easily impede nearfield coupling. Therefore, ahead of measurement, the nearfield signal is diverted by flip mirror and tuned with the help of near-IR detector. The nearfield microscope built in Data Acquisition unit DAQ and image processing software extract signal's high harmonics and a maximization is achieved by adjusting parabolic mirror focusing/collecting angle.

Considering the nanoscale of the target, the SH signal from the single nanostructure is supposed to be very weak. Addressing this challenge, we selected photomultiplier detector (PMT) which is capable to detect single photon. In our experiment H7422-40 photo sensor module from Hamamatsu™ was used. Besides the sensitivity to single photons, PMT detectors are not effective in wavelengths higher than 900 nm, hence it also behaves as a short pass filter, enhancing signal filtering. InGaAs detector from Newport™, suitable for near IR range was used for SNOM imaging.

3.2.3 Results

AFM together with nearfield images are depicted on Figure 33. It can be seen the light field ignited dipole mode in nanostructure. Obviously, the background noise is fading with turning to higher harmonics as it was suggested in Section 2.2.3. However, the price is that the nearfield signal is getting weaker, making a shot noise feasible. In the illustration below fifth harmonic signal picture is rather grainy

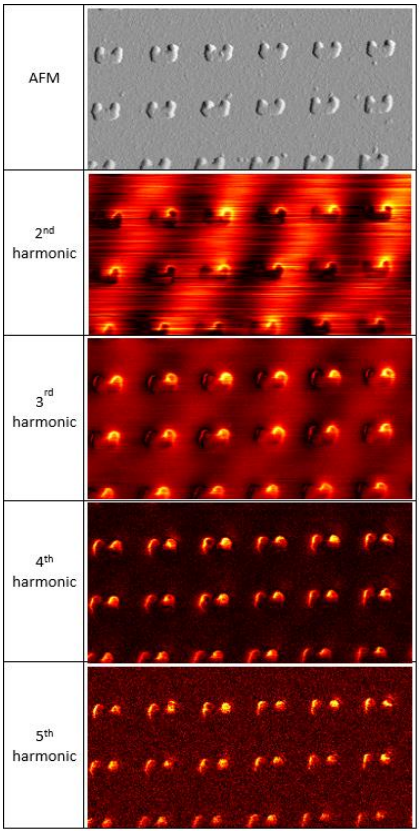

Figure 33 - AFM and demodulated to higher harmonics nearfield images of SRR with 140nm base and 80 nm legs Note the removed background pattern in 4th and 5th harmonics.

compared to the fourth harmonic. Typically, third or fourth harmonic order offer good compromise between background suppression and a signal strength.

To complete the picture of SNOM microscopy introduction, an artifact image is presented on Figure 34. On the figure (a) one can see AFM shadowed SRR. We assume that some tip fracture can behave as "parasitic" apex, and interacts with the sample. The resulted image from this interaction resembles SRR shadow. Clearly, this second apex also scatters a nearfield signal, so the "shadow" artifact appears on both AFM and SNOM images (Figure 34 (b)).

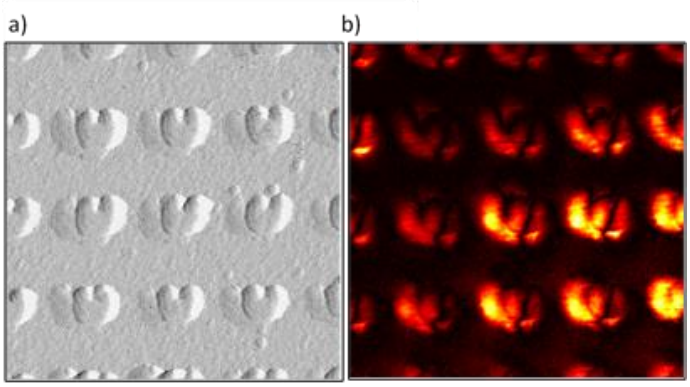

Figure 34 - Artifact in a) AFM and b) SNOM images.

Regarding the goal of the project that deal with measurement of second harmonic nearfield signal from nanostructure, it has not yet been achieved. There are two separate issues that hindered the results:

1. The SNOM microscope is equipped with built in data processing unit containing lock-in amplifier. Lock-in amplifier is capable to extract very low signals buried by detector and background noise level. This achieved by implying so called homodyne detection. First, the signal is demodulated by specific reference signal and by $\pi/2$ shifted reference signal. Then, both of demodulated signals are recombined and averaged over time. Since detector noise is uniform, the power is spread along broad spectrum and the noise amplitude level at reference frequency is low. Thus, integration over time is essentially wipes out all the signal frequencies differing from the reference frequency and the noise level is reduced drastically.

Depending on light level, the signal output from the photomultiplier tube can vary from continuous to discrete (see Figure 35). Recalling that second harmonic generation from the single nanostructure about 150 nm long is extremely low, the PMT tube outputs sequence of charge pulses. This nonperiodic comb of pulses introduced into lock-in amplifier are zeroed throughout time integration, because the signal at reference frequency is very low if not zero identical. As a result we did not recorded any signal at second harmonic frequency.

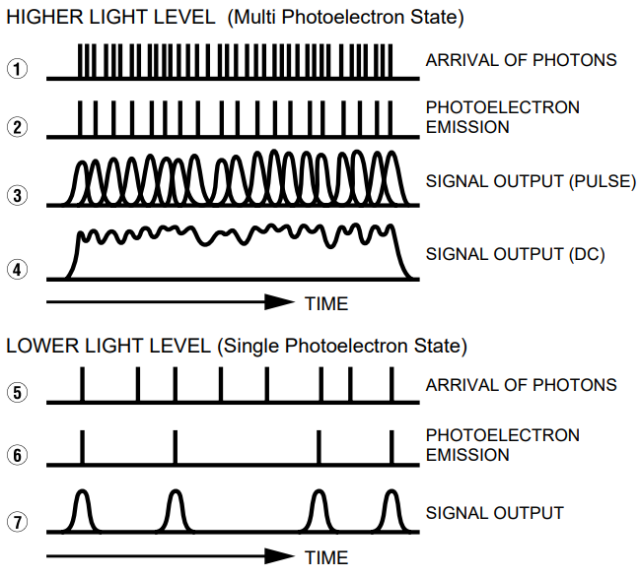

Figure 35 - Output signal from photomultiplier tube for high input light level in upper part and low input level in lower part of the image. For low level the output of PMT becomes a discrete sequence of pulses. Image from Hamamatsu™

2. To overcome signal loss described above, we ordered amplifier and discriminator unit, converting the photoelectron pulses output into 5V digital signals which are detectable by oscilloscope, bypassing the SNOM system built in reconstruction unit, that is to say the digital output is not feed into the Lock-in amplifier and therefore is not filtered out as it was described above. To our regret, internal failure of one piezo motors (not our fault) left no other option but to send the microscope for repair at manufacturer's site in Germany. The overall shipping in both ways and repair caused months of stalling and have not leaved the time to finish the project. Nevertheless, we think that the new detection approach will help the future researches to achieve the goal.

4. Summary

In current research we examined an application of nonlinear scattering theory to predict second harmonic response in metamaterials. The analysis was performed both numerically and experimentally. In numerical studies, we've found that the nonlinear scattering approach yields results compliant with previous experiments and simulations of parallel group. The nonlinear signal "bell curve" behavior was confirmed numerically and the optimal AS ratio was found to be ~0.2 for the straight corners SRR nanostructures, while Miller's rule based on Lorentz model gave an estimation of ~0.15. Furthermore, the strong dependence of nonlinear dipoles amplitudes and phases distribution along nanoparticle on asymmetry is with agreement to the previous work. Nevertheless, the percentage of amplitude and phase in total SHG is yet to be verified because of overlap integration might be screened by signal amplification around particle sharp corners.

In addition, the simulation of somewhat modified SRR nanoparticles together with the simulations of particles width and polarization angle effect on SHG provide additional degrees of freedom and give an insight into calculation of an optimal second harmonic response in defined light spectrum. Therefore, we believe that a future design of metamaterials trimmed to specific application such as frequency conversion and Raman sensing can benefit from this technique.

The use of Lumerical FDE solver also exposed several limitations in the computation of a nonlinear overlap integral. Specifically, the instability (particularly for shorter waves spectrum) at computation on the boundaries between a conducting and a dielectric materials. This "weak point" is accountable for excessive sensitivity to the small geometry changes, as in the case of the simulations over the nanostructures with a gradually increasing asymmetry ratio. To address the solver's computational limitations and strengthen the method validity we propose to repeat the calculations with the help of another commercially available FDE solver. In addition, we think that the simulation over the structures with rounded corners will emphasize the local dipoles vector sum cancelation by averting strong field amplification on the structure's corners. Last but not least, owing to its universality, the nonlinear scattering theory is not confined to solely SHG and can be utilized for higher harmonics signal prediction as well.

Regarding the experimental efforts, the near field second harmonic signal has remained elusive. Nevertheless, while working with SNOM microscope we earned a valuable experience in low signal detection, AFM and SNOM microscope routine both for visible and near IR part of the spectrum, an

integration of SNOM microscope with auxiliary optical components, a homodyne detection and its practical limitations for a digital signal output. All that said, will contribute to further experimental investigations. Once achieved, it will also allow to explore the nonlinearities of other nanostructures' geometries and higher order optical nonlinearities.

5. List of Figures

6. Bibliography

[1] R. W. Boyd, Nonlinear Optics, Academic Press, 2008.

[2] C. Garrett and F. Robinson, "Miller's phenomenological rule for computing nonlinear susceptibilities," *IEEE Journal of Quantum Electronics,* vol. 2, no. 8, pp. 328-329, 1966.

[3] S. Scandolo and F. Bassani, "Miller's rule and the static limit for second-harmonic generation," *Physical Review B,* vol. 51, no. 11, p. 6928–6931, 1995.

[4] C. Wenshan and V. Shalaev, Optical Metamaterials, New-York: Springer-Verlag, 2010.

[5] K. O'Brien, H. Suchowski, J. Rho, A. Salandrino, K. Boubacar, X. Yin and X. Zhang, "Predicting nonlinear properties of metamaterials from the linear response," *Nature Materials,* vol. 14, no. 4, pp. 379-383, 2015.

[6] S. Roke, M. Bonn and A. Petukhov, "Nonlinear optical scattering: The concept of effective susceptibility," *Physical Review B,* vol. 70, no. 115106, 2004.

[7] L. Novotny and B. Hecht, Principles of Nano-Optics, Cambridge: Cambridge University Press, 2012.

[8] F. Huth, "Nano-FTIR - Nanoscale Infrared Near-Field Spectroscopy," PhD Thesis UPV/EHU, San Sebastian, 2015.

[9] F. Keilmann and F. Hillenbrand, " Near-field optical microscopy by elastic light scattering from a tip.," *Philosophical Transactions of the Royal Society of London,* vol. 362, no. 1817, p. 787805, 2004.

[10] N. Ocelic, A. Huber and R. Hillenbrand, "Pseudoheterodyne detection for background-free near-field spectroscopy," *Appl. Phys. Lett.,* vol. 89, no. 10, p. 101124, 2006.

[11] R. Hillenbrand, B. Knoll and F. Keilmann, "Pure optical contrast in scattering-type scanning near-field microscopy," *Journal of Microscopy,* vol. 202, no. 1, pp. 77-83, 2001.

[12] C. F. Bohren and D. R. Huffman, Absorption and Scattering of Light by Small Particles, A Wiley-Interscience Publication , 1998.

[13] B. E. Saleh and M. C. Teich, Fundamentals of Photonics, Wiley-Interscience, 2007.

[14] A. J. Huber, F. Keilmann, J. Wittborn, J. Aizpurua and R. Hillenbrand, "Terahertz NearField Nanoscopy of Mobile Carriers in Single Semiconductor Nanodevices," *Nano Letters ,* vol. 8, no. 11, pp. 3766-3770 , 2008.

[15] M. G. Ruppert, D. M. Harcombe, M. R. Ragazzon, R. S. Moheimani and A. J. Fleming, "A review of demodulation techniques for amplitude-modulation atomic force microscopy," *Beilstein Journal of Nanotechnology,* vol. 8, pp. 1407-126, 2017.

[16] Y. Liu and X. Zhang, "Metamaterials: a new frontier of science and technology," no. 40, pp. 2494-2507, 2011.

הפקולטה למדעים מדויקים ע"ש ריימונד ובברלי סאקלר
בית ספר לפיסיקה ואסטרונומיה
המחלקה לחומר מעובה
אוניברסיטת תל אביב

יצירת אותות לא לינאריים מננו-חלקיקים

חיבור זה מוגש כחלק מהדרישות לקבלת תואר 'מוסמך למדעים' באוניברסיטת תל אביב

על ידי

אילן שר

עבודה זו הוכנה בהנחיתו של פרופ' חיים סוכובסקי

יוני 2019

תקציר

אופטיקה לא לינארית היא תופעה אשר מאופיינת בתגובה אופטית בתדר שונה מתדר הגל הפוגע. התופעה הלא לינארית, אשר התגלתה זמן קצר לאחר המצאת הלייזר, הובילה למאמצים לפתח בסיס תאורטי לתגובה הלא לינארית האופטית. המודל אשר פותח התמקד בעיקר בהכנסת הפרעות קטנות למודל הסטנדרטי של אוסילטור הרמוני, הידוע היום כמודל אוסילטור הרמוני הלא לינארי (NHO) הניב תוצאות טובות בחיזוי תגובה לא לינארית עבור חומרים רבים ובצורות הגימטריות שונות. עם זאת המודל הינו מוגבל לחומרים אי-אורגניים לא ליניאריים.

הניסויים שבדקו יצירת הסיגנלים בהרמוניה שנייה (SHG) ממטא-חומרים עם גיאומטריה משתנה נתנו תוצאותיהן שאינן תואמו לחיזוי מודל NHO. ברם, תוצאותיהן של תורת הפיזור הלא לינארית שפותחה בשנים האחרונות היו קונסיסטנטיות עם התצפית הניסיונית. לפי תורה הזו, האות הלא לינארי הכולל יהיה תלוי לא רק באמפליטודות הדיפולים המושרים על פני המטא-חלקיק אלא גם בפאזה ביניהם. כתוצאה מכך, האות המרבי מתקבל לא בהכרח ממטא-חלקיק עם התגובה הלא ליניארית החזקה ביותר, אלא מחלקיק שמשקלל אמפליטודה עם יכולת התאבכות בונה עבור הדיפולים המושרים על פניו.

מטרתה של עבודה זו הייתה לגלות אות SHG על פני השטח של ננו-חלקיקים באמצאות מיקרוסקופ שדה הקרוב (SNOM) מצומד ללייזר פולסים אולטרה מהירים (Femto Second laser). ההבחנה באות SHG חזק בשדה הקרוב מחלקיק מסוג (nanobar) ביחד עם עובדה שבשדה הרחוק תגובת SHG שלו זניחה, תהווה הוכחה לתורת הפיזור הלא לינארית ותשמש ככלי עזר יעיל לפיתוח עתידי של מטא-חומרים עם תגובות לא לינאריות רצויות.